Quaternary Science Reviews 204 (2019) 187–207

Contents lists available at ScienceDirect

Quaternary Science Reviews

journal homepage: www.elsevier.com/locate/quascirev

Marine Isotope Stage 4 in Australasia: A full glacial culminating 65,000 years ago – Global connections and implications for human dispersal

Patrick De Deckker [a, *], Lee J. Arnold [b], Sander van der Kaars [c, d], Germain Bayon [e], Jan-Berend W. Stuut [f], Kerstin Perner [g, h], Raquel Lopes dos Santos [i], Ryu Uemura [j], Martina Demuro [b]

[a] Research School of Earth Sciences, The Australian National University, Canberra, ACT, 2601, Australia
[b] School of Physical Sciences, The Environment Institute and the Institute for Photonics and Advanced Sensing, University of Adelaide, Adelaide, South Australia, 5005, Australia
[c] School of Earth, Atmosphere and Environment, Monash University, Clayton, VIC, 3800, Australia
[d] Cluster Earth & Climate, Faculty of Earth and Life Sciences, Vrije Universiteit, 1081 HV, Amsterdam, Netherlands
[e] IFREMER, Marine Geosciences Unit, CS 10070, 29280, Plouzané, France
[f] NIOZ - Royal Netherlands Institute for Sea Research, Utrecht University, P.O. Box 59, 1790 AB, Den Burg, the Netherlands
[g] Uni Research Klima & Bjerknes Centre for Climate Research, Jahnebakken 5, 5033, Bergen, Norway
[h] Leibniz Institute for Baltic Sea Research, 15 Seestrasse, 18119, Rostock, Germany
[i] British Geological Survey, Centre for Environmental Geochemistry, Keyworth, Nottingham, NG12 5GG, UK
[j] Department of Chemistry, Biology, and Marine Science, University of the Ryukyus, 1 Senbaru, Nishihara, Okinawa, 903-0213, Japan

ARTICLE INFO

Article history:
Received 20 June 2018
Received in revised form
13 October 2018
Accepted 14 November 2018

Keywords:
Sea-surface temperature
Sea level
LGM
MIS4
Glaciation
Human migration
Airborne dust
Deuterium excess
Single-grain OSL dating
Penultimate glaciation
STCZ

ABSTRACT

Over the last four decades of palaeoclimate research, significant emphasis has been placed on the Last Glacial Maximum (LGM) spanning 26.5–19 thousand years ago (ka), a period that saw significant (~125 m) sea-level reductions and major ice caps adorning large parts of the Northern Hemisphere. Here, we present evidence for another major glacial period spanning 71–59 ka (Marine Isotope Stage 4: MIS4) from a well-dated marine sequence offshore South Australia. The astronomically-tuned chronology of this deep-sea core is confirmed using single-grain optically stimulated luminescence dating (OSL), providing confidence in our high-resolution age model. Our approach to the study of our MD03-2607 core has been to employ many different proxies. These are: $\delta^{18}O$ of both planktic and benthic foraminifera for stratigraphic purposes, faunal counts of planktonic foraminifera to reconstruct the position of oceanic fronts and currents, alkenone palaeothermometry, XRF core scanning to determine the presence of aeolian dust, and εNd isotope to identify fluvial discharge over the core site. We compare our new proxy findings with other archives for mainland Australia and Tasmania.

Our multi-proxy palaeoclimate reconstructions are consistent with other marine, terrestrial and cryosphere archives across the Southern Hemisphere and suggest, for the first time, that MIS 4 was almost as dramatic as the LGM. During MIS4, global sea-level was reduced by ~100 m, glaciers across Australasia were more significant compared to the LGM, and sea-surface temperatures were much reduced. These glacial conditions uniformly peaked around 65 ka. Global comparisons show major glacial conditions and vegetation shifts elsewhere during MIS4, but many are poorly dated. The significant environmental changes taking place during this glacial period were paralleled by waves of human dispersal across Eurasia and the earliest evidence of human occupation in northern Australia at 65 ka.

© 2018 Elsevier Ltd. All rights reserved.

1. Introduction

The terminology of the various glacial and interglacial stages of the Late Pleistocene were first coined by Emiliani (1955) based on his comparison of deep marine isotope records and continental stratigraphies. At the time, Stage 2 – which was to later be called later the Last Glacial Maximum (LGM) – Marine Isotope Stage 2 (MIS), was considered to relate to the maximum glacial extent in Europe (Würm III/II) and North America (Wisconsinian). Stage 4 (Emiliani (1955: Fig. 15) was thought to relate to the Würm I phase, which had already been well documented but not adequately

* Corresponding author.
E-mail address: patrick.dedeckker@anu.edu.au (P. De Deckker).

https://doi.org/10.1016/j.quascirev.2018.11.017
0277-3791/© 2018 Elsevier Ltd. All rights reserved.

dated. Since this seminal work (Emiliani, 1955), MIS4 has been considered to represent a period of substantial cooling in the global ocean related to a significant sea-level drop, but it has never been considered to be a true glacial period, in particular in the northern hemisphere.

Significant emphasis has been placed on reconstructing the LGM conditions for the entire globe over recent decades by the CLIMAP group (1976) and MARGO (Kucera et al., 2005)). In contrast, the MIS4 marine sedimentary record has remained poorly investigated because this period lies beyond the conventional limits of radiocarbon dating. Recently, marine core dating has improved in reliability owing to better correlations with the astronomically-tuned benthic foraminifera $\delta^{18}O$ stack curves (Liesicki and Raymo, 2005; Liesicki and Stern, 2016). Advances in other geochronology applications have also fuelled improved MIS4 reconstructions, such as U/Th dating of corals on exposed [tectonically uplifted] or drowned [obtained through coring] marine terraces. In addition, long sequences recovered from cave speleothems have been studied using a variety of dating and palaeoclimate proxy techniques, and have produced high-precision temperature, evaporation and precipitation reconstructions for MIS4.

Recent cosmogenic exposure dating studies of MIS4 glacial stratigraphies in the Australasian region have highlighted an important observation: the extent of glacial advances between the LGM and MIS4 are such that MIS4 moraines were more extensive than LGM moraines (6–8). The implications of these findings are significant for our interpretation of MIS4 climates, and a reassessment of this climatic stage appears timely in light of new and emerging palaeoenvironmental evidence.

To this end, we present detailed reconstructions of the timing and climate of MIS4 recorded in a deep-sea core MD03-2607 taken from offshore southern Australia. We compare results obtained using various proxies for this period, and compare our findings with other related MIS4 reconstructions from the Australasian region and Antarctica. We focus, in particular, on sea-surface temperature reconstructions using alkenone palaeothermometry, foraminiferal faunal analyses to determine regional sea conditions (the position of various oceanic fronts and currents, as well as depth of the thermocline), proxies of aeolian dust and fluvial sediment discharge at sea, and pollen-based reconstructions of terrestrial vegetation and regional rainfall.

Our palaeoclimatic data, when compared with terrestrial archives from central Africa and Europe, show that MIS4 was a period of broad vegetation changes, ranging from arid conditions in Africa to steppe conditions in parts of Europe. These global habitat changes are likely to have placed significant ecological pressures on modern human populations in Africa and, coupled with an extensive sea-level drop, would have favoured human dispersal out of Africa and across the frontier continents of Eurasia and Australasia (Timmermann and Friedrich, 2016; Tierney et al., 2017; Norman et al., 2018; Bird et al., 2018).

2. Materials and methods

2.1. Deep-sea core MD03-2607

Deep-sea core MD03-2607 was taken on a gentle slope south of the upper Sprigg Canyon at 865 m water depth (Fig. 1). It consists of 32.95 m of foraminiferal silty sand, intercalated with silty clay sections. The core is located at 36°57'64"S, 137°24'39"E, almost due south of Kangaroo Island (Hill et al., 2005) (Fig. 1). Airborne quartz grains are found in most samples of the core as the site is below the flow path as can be dust plumes, witnessed today (De Deckker et al., 2010). The chronology of the core has already been presented by Lopes dos Santos et al. (2012, 2013a,b) but, with additional samples,

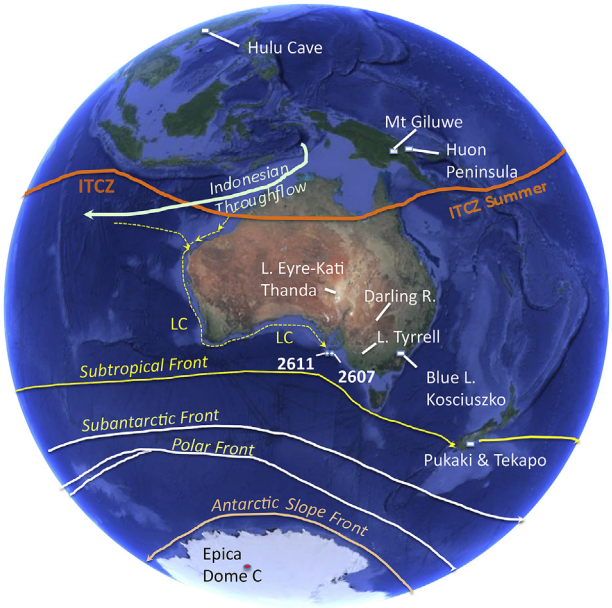

Fig. 1. Satellite image taken from Google Earth® showing the locations of all the sites mentioned in the text, as well as the position of ocean boundaries and currents. LC = Leeuwin Current, ITCZ= Intertropical Convergence Zone.

it has been updated in the present study using the new benthic stack record (Liesicki and Stern, 2016).

Core 2607 has previously been the subject of several studies (Gingele and De Deckker, 2004, 2005; Gingele et al., 2007; De Deckker et al., 2010, 2012; Lopes dos Santos et al., 2012, 2013a; 2013b; Bayon et al., 2017). These studies all indicate that the core does not contain any hiatuses, and that it benefits from a satisfactory sedimentation rate [considering the Australian region, which lacks tectonic activity and glacial erosion] as it is located opposite the mouth of the River Murray (the end point of the Murray Darling Basin that covers just over 1×10^6 km^2). Ancestral meanders of the Murray are known to have spread onto the Lacepede Shelf during periods of low sea levels, meaning that, at some stages in the past, the core site was only 40 km from the coastline compared to being almost 200 km from the mainland today (Hill et al., 2005).

All of the samples analysed from the core were taken from 1 cm thick intervals, except for the main OSL samples, which required more material (see details below). On average, a single 1 cm-thick sample taken from the 75 to 55 ka section of the core studied in this paper represents ~80 years of sedimentation.

2.2. Core chronology

2.2.1. $\delta^{18}O$ analyses on foraminifera

Building on Lopes dos Santos et al. (2012) results, we have performed a series of additional analyses of planktic and benthic foraminifera from MD03-2607. Samples were analysed following the methods detailed in Spooner et al. (2011) and Lopes dos Santos et al. (2012). Due to the scarcity of benthic foraminifera taxa in the sampled intervals, we relied on analyses of two distinct groups (*Planulina wuellerstorfi* and *Uvigerina* sp.) and applied a correction factor of −0.3‰ to all analyses of the latter species following Hooghakker et al. (2010).

2.2.2. $\delta^{18}O$ stratigraphy

The chronology for core MD03-2607 (hereafter called 'core 2607') (Lopes dos Santos et al., 2012, 2013a) relied on a large

number of radiocarbon ages for the upper portion of the core, and was confirmed by a series of optically stimulated luminescence (OSL) ages. To constrain the chronology of the MIS4 to MIS 6 section of the core, Lopes et al. (2013a) used numerous tie points linked to the benthic foraminifera stack curve (Liesicki and Raymo, 2005). We have now updated this age model by using the benthic foraminifera stack record for Pacific intermediate waters (Liesicki and Stern, 2016) on the assumption that, even if our core is located in the far eastern side of the Indian Ocean, the intermediate waters bathing our core site would originate from the southern part of the Tasman Sea (Middleton and Bye, 2007). This approach was favoured over using the benthic stack record for Indian Ocean intermediate waters (Liesicki and Stern, 2016) as these authors only used 3 records from the eastern Indian Ocean and these are located to the NW of Australia. We have used tie points linking key step changes in our core with the Pacific intermediate waters (Liesicki and Stern, 2016) curve, and have calculated an age for every depth of the core down to 12 m. The resultant age-depth data are plotted in Fig. 2. The veracity of the age model is tested below using OSL age dating of individual horizons in the core.

2.3. Single-grain optically stimulated luminescence (OSL) dating procedures

Six intervals of the core have additionally been radiometrically dated as part of the study using single-grain OSL, with the aim of independently assessing the veracity of the new isotopic age model obtained from the benthic stack record. OSL samples were collected from targeted horizons that were considered to encompass MIS4, using tie points derived from the benthic foraminifera stack curve of Liesicki and Stern (2016). Full details of the OSL dating procedures are provided in the online Supplementary Information section. Six OSL dating samples were collected from pre-split core sections that had been kept in a temperature- and moisture-controlled storage facility (at 4 °C) at the Australian National University since collection at sea. The OSL dating samples were collected from the un-illuminated centres of the cores under safe (dim red filtered) light conditions. Quartz grains of 63–90 μm and 90–180 μm diameter were prepared for burial dose estimation using standard procedures (e.g. Demuro et al., 2013), including heavy liquid density separation at 2.72 g/cm^3 and 2.62 g/cm^3, and a 48% hydrofluoric acid etch (40 min) to remove the alpha-irradiated outer layers of the quartz extracts. OSL measurements were made using the experimental apparatus described in Arnold et al. (2013, 2016). Equivalent dose (De) values were determined using the single-aliquot regenerative-dose (SAR) procedure (Murray and Wintle, 2000) shown (as well as discussed) in Supplementary Table S1. Between 600 and 1900 single-grain De measurements were made for each sample. Individual De values were only included in the final age calculation if they satisfied a series of standard and widely tested quality-assurance criteria, as detailed in Arnold et al. (2013, 2016). Sensitivity-corrected dose-response curves were constructed using the first 0.17 s of each green laser stimulation after subtracting a mean background count obtained from the last 0.25 s of the signal. Between 600 and 1900 single-grain De measurements were made for each sample.

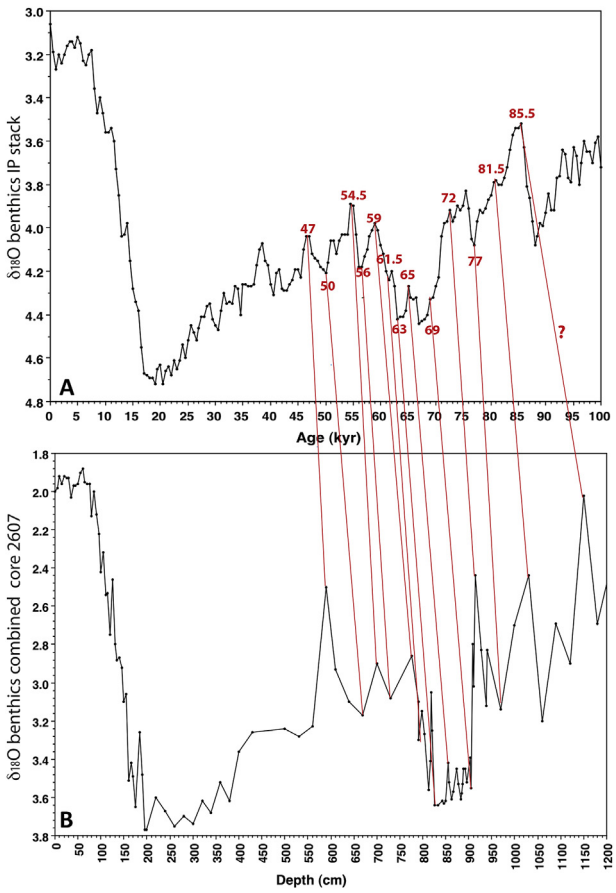

Fig. 2. Correlation between the benthic foraminifera stuck curve (Liesicki and Stern, 2016) for Intermediate Waters for the Pacific Ocean and the benthic foraminifera $\delta^{18}O$ for core 2607 showing the tie points which were used to provide ages for intervals spanning the 75 to 55 ka interval. Ages were then calculated between the tie points assuming a constant sedimentation rate between the tie points.

Owing to well-documented dosimetric complexities in marine sedimentary environments, we have calculated the final OSL ages of the MD2607 samples using an iterative dose rate model that takes into consideration both the time-independent (lithogenic and authigenic parent) activities of the ^{238}U series, ^{235}U series, ^{232}Th series and ^{40}K series, and the time-dependent (scavenged and authigenic daughter) activities of the ^{238}U and ^{235}U series. These dose rate calculations have been derived using the Marine$_{xs+auth}$ model described in Armitage (2015), which has been modified to incorporate the time-dependent scavenged ^{230}Th correction detailed in Henderson and Anderson (2003) and an additional time-dependent correction for the in-growth of ^{230}Th from authigenic ^{234}U during the burial period (see Supplementary Information for further details). Radionuclide specific activities have been converted to beta and gamma dose rates using the published conversion factors of Guerin et al. (2011), allowing for beta-dose attenuation (Mejdahl, 1979; Brennan, 2003) and long-term water content correction (Aitken, 1985). To estimate the long-term average water content for the single-grain OSL samples, we have used 'as measured' values determined separately for the beta and gamma dose rate bulk sediment samples (see Supplementary Table S3). The measured water contents for MD03-2607 are considered to be sufficiently representative of those at the time of core extraction, as the cores have remained sealed and refrigerated at 4 °C since their collection. A relative uncertainty of 10% has been assigned to these long-term moisture estimates to accommodate any minor variations in hydrologic conditions during burial or prior to sampling.

2.4. Planktic foraminifer counts

Planktic foraminifers were counted from 27 samples that cover the MIS4 portion of core MD03-2607. For each sample, c. 10 g of dry sediment was wet sieved through a 150 μm sieve and the residue was subsequently dried at 45 °C. Identification down to species

level (>150 μm), using a stereomicroscope, followed the nomenclature established in Parker (1962). A minimum of 350 specimens were counted from the dry residue per sample. Further details of the sample preparation and counting methods are provided in the supplementary sections of De Deckker et al. (2012) and Perner et al. (2018). The same planktic foraminiferal assemblage described in De Deckker et al. (2012) for LGM samples in the nearby core MD03-2611 were recognized in core MD03-2607. The assemblage is characterised by high abundance of *Globigerina bulloides* (av. 40%), followed by *Globorotalia inflata, Neogloboquadrina incompta,* and *Turborotalita quinqueloba* (av. 15%), *Turborotalita truncatulinoides* (av. 10%) and *Globigerinoides ruber* (av. 5%). Minor abundances (>av. 5%) of *Neogloboquadrina pachyderma, Globorotalia glutinata, G. scitula* and *G. hirsuta* are recorded.

2.5. Alkenone palaeothermometry

Alkenone ($U^{K'}_{37}$) analyses were performed on additional samples to complement the data already published (Lopes et al., 2013a, 2013b), and to obtain a higher-resolution record spanning MIS4. The additional alkenone samples were analysed at the British Geological Survey, on a Hewlett Packard 6890 GC equipped with flame ionization detection (FID) and fitted with an Agilent DB-1ms UI column (60 m × 0.25 mm id., 0.1 μm film thickness), using a similar method to that described in Lopes et al. (2012). Sea-surface temperatures (SST) were then reconstructed using the calculation of $U^{K'}_{37}$ proxy, which has previously been defined for core 2607 (Lopes et al., 2013a, 2013b).

2.6. Palynological analyses

The samples were processed following the same procedures for marine sediment samples described for another core offshore northwestern Western Australia by van der Kaars and De Deckker (2002).

2.7. Geochemical analysis of the sediments [Nd isotopes]

Prior to neodymium isotope analyses, bulk sediments were treated chemically to remove biogenic, Fe–Mn oxyhydroxide and organic components (Bayon et al., 2002). Clay-size fractions were separated from residual detrital material using low-speed centrifugation and digested by alkaline fusion (Bayon et al., 2015). Neodymium was isolated using conventional ion chromatography and isotopic measurements were performed at the Pôle Spectrométrie Océan (Brest), using a Thermo Scientific Neptune multi-collector ICPMS. Nd isotopic compositions were determined using sample-standard bracketing, by analysing JNdi-1 standard solutions every two samples. Mass-bias corrected values for $^{143}Nd/^{144}Nd$ were normalized to a JNdi-1 value of $^{143}Nd/^{144}Nd = 0.512115$ (Tanaka et al., 2000). Repeated analyses of JNdi-1 solution during the course of this study gave $^{143}Nd/^{144}Nd$ of 0.512106 ± 0.000005 (2 SD, n = 22), corresponding to an external reproducibility of ~ ±0.10ε (2 SD). Epsilon Nd values (εNd) were calculated using $^{143}Nd/^{144}Nd = 0.512630$ (Bouvier et al., 2008).

2.8. XRF scanning of the core

A 2 cm × 2 cm u-channel was taken from the entire core and elemental composition was obtained following the procedure detailed in Stuut et al. (2014) using an Avaatech XRF core scanner at 1-cm resolution at the Royal Netherlands Institute for Sea Research (NIOZ), following established methods (Stuut et al., 2014). Detailed bulk-chemical composition records acquired by XRF core scanning allow accurate determination of stratigraphic changes as well as assessment of the contribution of the various components in lithogenic and marine sediments. The core was measured at both 10 kV and 30 kV for 51 elements (Al, Si, P, S, Cl, K, Ca, Sc, Ti, V, Cr, Mn, Fe, Co, Ni, Cu, Zn, Ga, Ge, As, Se, Br, Rb, Sr, Y, Zr, Nb, Mo, Tc, Ru, Rh, Pd, Ag, Cd, In, Sn, Sb, Te, I, Cs, Ba, Hf, Ta, W, Re, Os, Ir, Pt, Au, Hg, Tl, Pb). Log-ratios of two elements measured by XRF core scanning can be interpreted as the relative concentrations of two elements and minimizes the effects of down-core changes in sample geometry and physical properties (Weltje and Tjallingii, 2008). It is now well established that the elements Ca, Fe, and Ti (of interest here) can be measured reliably with the XRF-scanning method (Tjallingii et al., 2007).

3. Results

3.1. Core MD03-2607 and its chronology

The chronology of core MD03-2607 has previously been presented (Lopes dos Santos et al., 2012, 2013a) but it has been updated here with additional samples, using the new benthic stack record (Liesicki and Stern, 2016). Correlation between the latter benthic foraminifera stuck curve for Intermediate Waters for the Pacific Ocean and the benthic foraminifera $\delta^{18}O$ for core 2607 using tie points was used to provide ages for intervals spanning the 75 to 55 ka interval (Fig. 2). Ages were then calculated between the tie points assuming a constant sedimentation rate between the tie points.

The single-grain D_e OSL dating results are summarised in Table 1. Between 6 and 10% of the De values measured per sample were considered suitable for OSL dating purposes after applying the single-grain quality assurance criteria of Arnold et al. (2013, 2016) (Table S2). Fig. S2 shows representative OSL dose-response and decay curve for grains that passed the SAR quality assurance criteria and were used for dating purposes. The single-grain D_e distributions of each sample is shown as a radial plots in Fig. 3, and discussed in further detail in the Supplementary Information. Four of the samples (MD2607-1, MD2607-2, MD2607-3 and MD2607-5) display low to moderate D_e scatter (Fig. 3a, c, d, e) and moderate overdispersion of 20–25% (Table 1). These D_e characteristics are considered to be indicative of adequate signal resetting prior to deposition and an absence of significant post-depositional mixing thereafter (Arnold and Roberts, 2009). Sample MD2607-4 displays moderate scatter and a higher overdispersion of 34 ± 5% (Fig. 3b); though the latter is consistent at 2σ with the overdispersion values obtained for the four well-bleached and unmixed surrounding samples from core MD03-2607. The final D_e values of samples MD2607-1, MD2607-2, MD2607-3 and MD2607-5 have been derived using weighted mean D_e estimates, calculated using the central age model (CAM) of Galbraith et al. (1999) (Table 1). The lowermost sample (MD2607-6) exhibits a positively skewed D_e distribution and a high overdispersion value of 45 ± 5% (Fig. 3f), which does not overlap at 2σ with the overdispersion values obtained for the four well-bleached and unmixed samples from core MD03-2607 (Table 1). These D_e distribution characteristics are consistent with those commonly reported for heterogeneously bleached single-grain OSL samples (e.g., Olley et al., 1999, 2004; Bailey and Arnold, 2006; Arnold et al., 2007; 2008, 2009). Comparisons of De estimates obtained from the fast-dominated and slow-dominated components of the OSL signal (Fig. S3) confirm the presence of heterogeneously bleached grains in the lowermost sample (see discussions in the Supplementary Information). We have therefore calculated the final D_e value for sample MD2607-6 using the minimum age model (MAM) of Galbraith et al. (1999) (Table 1).

The final OSL ages calculated using the iterative dose rate model

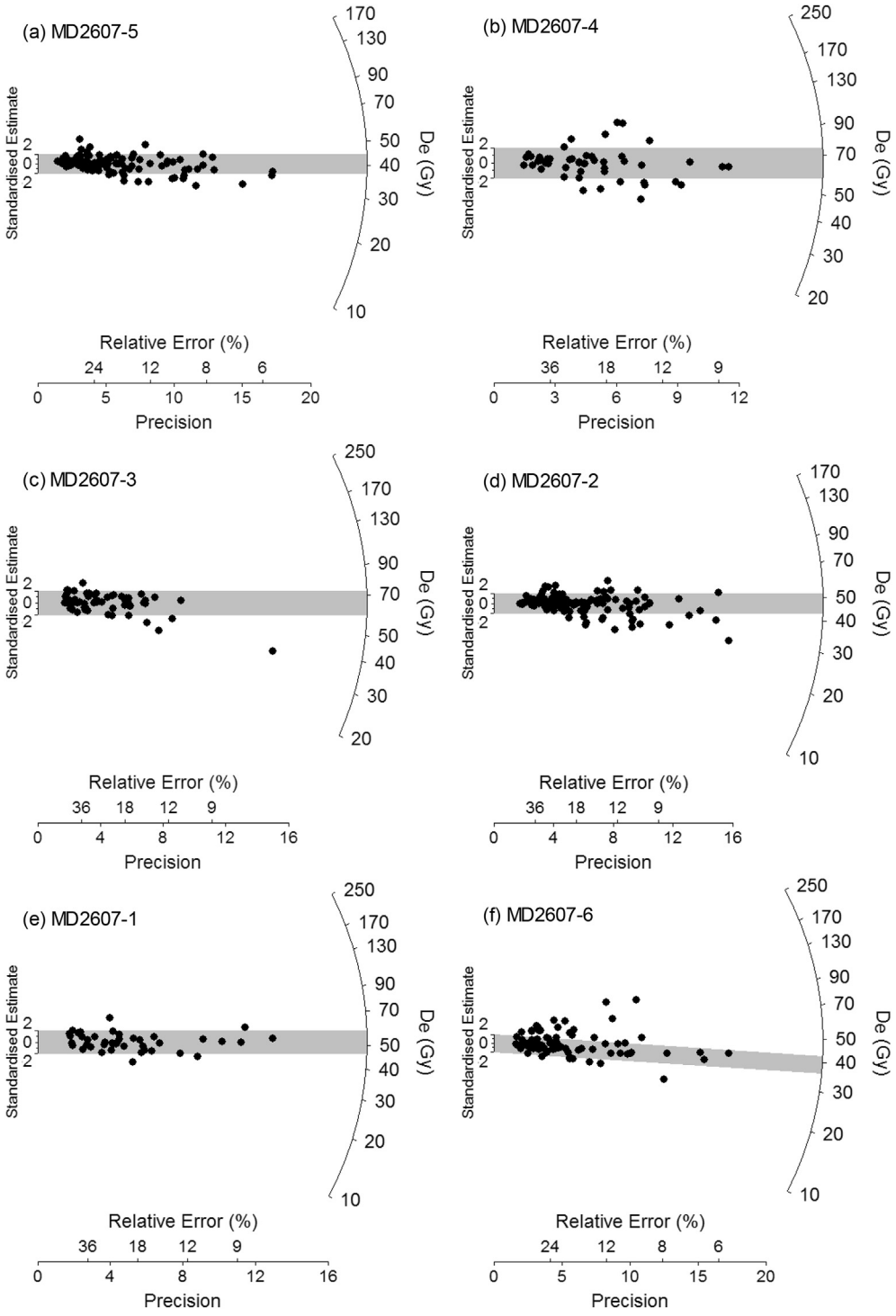

Fig. 3. Single-grain OSL D_e distributions for the six OSL samples taken from core MD03-2607, shown as radial plots (in order from highest core position to lowest core position). The measured D_e (in Gy) for an individual grain can be read by tracing a line from the y-axis origin through the point until the line intersects the radial axis (log scale) on the right-hand side. The corresponding standard error for this estimate can be read by extending a line vertically to intersect the x-axis. The x-axis has two scales: one plots the relative standard error of the D_e estimate (in %) and the other ('Precision') plots the reciprocal standard error. Therefore, values with the highest precisions and the smallest relative errors plot closest to the radial axis on the right of the diagram, and the least precise estimates plot furthest to the left. The grey shaded band on each plot is centred on the D_e value used for the final age calculation. For samples MD2607-1 to MD2607-5, this D_e value was calculated using the central age model (CAM) of Galbraith et al. (1999). For sample MD2607-6, the final D_e value was calculated using the four parameter minimum age model (MAM-4) of Galbraith et al. (1999).

(see Supplementary Information) are presented in Table 1 and shown in Fig. 4A. Although the six OSL ages have relatively large associated uncertainty ranges, it is evident that, at 2σ, these radiometric dating results are consistent with the isotopic age assignments of individual layers based on the benthic stack record. Three of the independently dated horizons, OSL MD2607-1 (core depth 912–917 cm), OSL MD2607-2 (core depth 904–909 cm) and OSL MD2607-3 (core depth 872–878 cm), returned mean OSL ages

Table 1
Single-grain D_e summary statistics, age model results, modelled dose rate data, and final ages for the six OSL dating samples taken from core MD03-2607.

OSL Sample ID	Core depth (cm)	Grain size (μm)	Modelled dose rate data		Equivalent dose (D_e) data					OSL age (ka)[b,h,i]
			Time-independent dose rate (Gy/ka)[a,b]	Total dose (xs + xa in-growth) (Gy)[b,c]	n/N[d]	Overdis-persion (%)[e]	Age Model[f]	L_{max} score[g]	D_e (Gy)[b]	
MD2607-5	782–787	90–180	0.37 ± 0.03	20.4 ± 1.9	125/1300	21 ± 2	CAM		41.1 ± 1.1	55.5 ± 3.5
MD2607-4	844–849	63–180	0.66 ± 0.04	22.6 ± 2.2	51/700	34 ± 5	CAM	−27.76	65.5 ± 3.9	**65.5 ± 5.1**
			0.66 ± 0.04	19.2 ± 2.8			MAM-3	−26.70	55.4 ± 6.8	55.2 ± 7.3
			0.66 ± 0.04	20.1 ± 1.9			MAM-4	−25.94	57.9 ± 3.2	57.8 ± 4.3
MD2607-3	872–878	90–180	0.54 ± 0.04	29.6 ± 2.8	60/600	25 ± 4	CAM		65.4 ± 3.1	**66.6 ± 4.7**
MD2607-2	904–909	90–180	0.31 ± 0.03	25.6 ± 2.2	127/1900	24 ± 2	CAM		47.4 ± 1.3	**69.7 ± 4.5**
MD2607-1	912–917	63–180	0.31 ± 0.03	30.0 ± 2.9	42/700	20 ± 4	CAM		52.1 ± 2.4	**70.6 ± 5.2**
MD2607-6	1014–1019	90–180	0.22 ± 0.02	26.1 ± 2.7	84/1300	45 ± 5	CAM	−65.10	48.4 ± 2.7	99.4 ± 8.4
			0.22 ± 0.02	20.5 ± 2.2			MAM-3	−56.13	37.3 ± 2.0	75.3 ± 6.3
			0.22 ± 0.02	21.5 ± 2.0			MAM-4	−52.56	39.3 ± 1.4	**79.4 ± 5.7**

[a] The time-independent dose rate component of the $Marine_{xs+auth}$ model was determined from the measured lithogenic ^{40}K,^{232}Th and ^{235}U activities, the calculated lithogenic ^{238}U activities (measured ^{238}U activities minus authigenic $^{238}U_{xa}$ activities), and the calculated authigenic uranium (U_{xa}) activities for the pre-^{230}Th part of the decay series (see Supplementary Information for full details).

[b] Mean ± total uncertainty (68% confidence interval), calculated as the quadratic sum of the random and systematic uncertainties.

[c] The total modelled dose derived from scavenged $^{230}Th_{xs}$ and $^{231}Pa_{xs}$ since burial, and progressive in-growth of $^{230}Th_{xa}$ from authigenic $^{234}U_{xa}$ decay during the burial period (see Supplementary Information for full details).

[d] Number of D_e measurements that passed the SAR rejection criteria (n)/total number of grains analysed (N).

[e] The relative spread in the D_e dataset beyond that associated with the measurement uncertainties for individual D_e values, calculated using the central age model (CAM) of Galbraith et al. (1999).

[f] Age model used to calculate the sample-averaged D_e value for each sample. CAM = central age model; MAM-3 = 3-parameter minimum age model; MAM-4 = 4-parameter minimum age model (Galbraith et al., 1999). MAM-3 and MAM-4 D_e estimates were calculated after adding, in quadrature, a relative error of 20% to each individual D_e measurement error to approximate the underlying dose overdispersion observed in 'ideal' (well-bleached and unmixed) sedimentary samples from this core (i.e., samples MD2607-1, MD2607-2, MD2607-3 and MD2607-5) and from global overdispersion datasets (Arnold and Roberts, 2009).

[g] L_{max} represents the maximum log likelihood score of the CAM, MAM-3 or MAM-4 fit. For a given sample, the L_{max} score of the MAM-3 is expected to be substantially higher (i.e. at least 1.92 greater) than that of the CAM when the addition of the extra model parameter improves the fit to the data. Likewise, the L_{max} score of the MAM-4 is expected to be significantly greater than that of the MAM-3 (by at least 1.92 when compared with the 95% C.I. of a X^2 distribution) when the addition of the extra model parameter improves the fit to the data. If the extra parameter of the MAM-3 (or MAM-4) is not supported by the data, then its L_{max} score will be similar to (i.e. within 1.92 of) the CAM (or MAM-3) L_{max} score, indicating that the simpler age model explains the data equally well (Arnold et al., 2009). The MAM-3, MAM-4 and LLIK ratios were not applied to samples MD2607-1, MD2607-2, MD2607-3 and MD2607-5, as the overdispersion value of these three samples are all within ±2σ of 20% (the global average for fully bleached and undisturbed samples; Arnold and Roberts, 2009) and are considered to be well-bleached.

[h] Total uncertainty includes a systematic component of ±2% associated with laboratory beta-source calibration.

[i] The preferred age is shown in bold. For samples MD2607-4 and MD2607-6, the preferred age has been derived using the statistical age model that yielded the optimum L_{max} score, following the criterion outlined in footnote g and Arnold et al. (2009) (see Supplementary Information text for further details).

that plot almost exactly on the age curve obtained by correlation with the data of Liesicki and Stern (2016) (Fig. 3A and B). Although the mean OSL ages for the other three samples (see Table 1) plot away from the isotopic age-depth curve (Fig. 4A and B) they are still consistent with the isotopic data at their 2σ confidence intervals. Overall, the additional single-grain OSL chronology obtained in this study supports the isotopic age assignments obtained via correlation with benthic stack record (Fig. 2A and B), and provides added confidence in our age model. Owing to the superior precision of the age assignments obtained from the benthic foraminifera stack, we have used this data here to assign final ages to individual horizons in core MD03-2607.

For the purpose of data presentation, we include all proxy results obtained for the 75 to 55 ka section of core MD03-2607, to ensure that we encompass all of the previously considered age ranges for MIS4 (Fig. 4B).

3.2. The $\delta^{18}O$ composition of the benthic foraminifera

The $\delta^{18}O$ composition of the benthic foraminifera in core MD03-2607 shows a surprising two-step change (at 72 ka and a second one at 70 ka) from lighter to heavier composition (Fig. 5A). Heavy values were maintained until 62.8 ka with a shift to lighter values completed by 62.5 ka. While our record is restricted due to the paucity of material available for analysis, the consistency of the OSL ages provides added.

The $\delta^{18}O$ composition of the planktic foraminifer *Globigerina bulloides* from the 75-55 ka time interval is displayed in Fig. 5B. A clear signal change is recognized at 70.8 ka, which is marked by a rapid drop on the order of ~0.75‰. Thereafter, heavier $\delta^{18}O$ values fluctuated until a shift towards lower values occurred after 60.5 ka and was maintained until 58.7 ka.

3.3. Sea-surface temperature reconstructions

Sea-surface temperatures (SST) based on alkenone thermometry appear stable at ~17 °C prior to 70.9 ka, and were followed by a rapid drop of ~1 °C within ~600 years and the trend continued until 68 ka (Fig. 5E). By this time, SSTs had dropped more than 4 °C. Eventually, by 63 ka, SST had risen again by some 2 °C, reaching its lowest value of 12.6 °C at 66.8 ka. Subsequently, SST fluctuated and eventually rose to pre-MIS4 values (17.2 °C) by 58.6 ka.

3.4. The Leeuwin Current

The most significant planktic foraminifera observed in samples spanning the 75 to 55 ka interval is *Globigerinoides ruber*. This small taxon is a clear indicator of the presence of the Leeuwin Current above the core site (De Deckker et al., 2012). Fig. 5D shows that *G. ruber* percentages lay above 15% just before 72 ka and then dropped to almost zero by 68.25 ka. The almost total absence of this species in the core is maintained until 64 ka, with percentages still remaining low still until 60 ka. After this time, *G. ruber* percentages increased rapidly to reach values similar to those observed before MIS4 commenced. A strong correlation between *G. ruber* percentages and SST is therefore evident over the 75-55 ka record (Figs. 5D–E, 6).

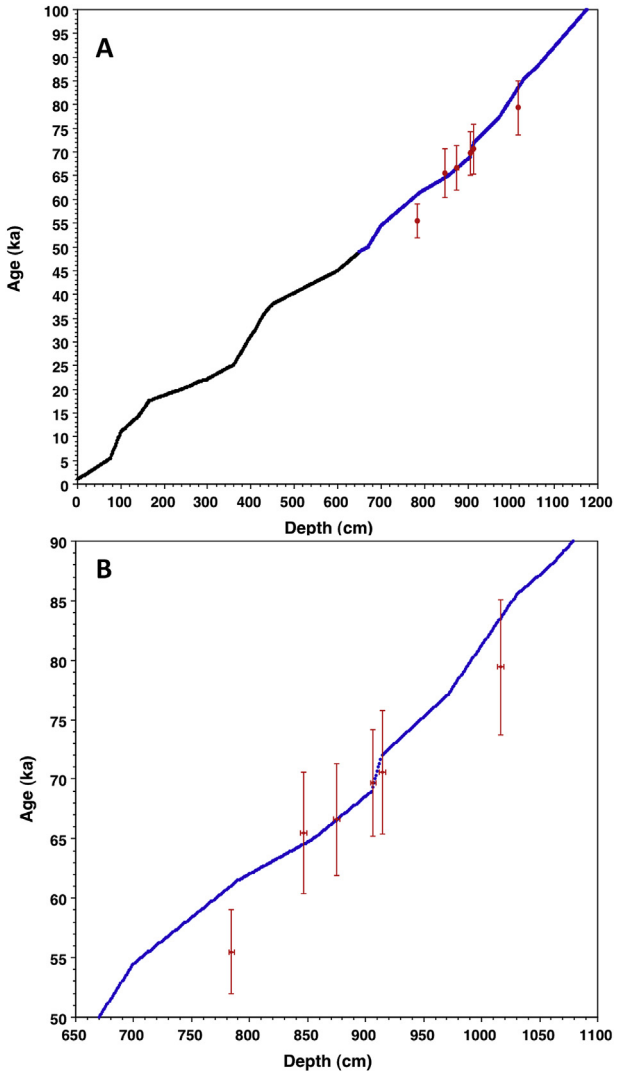

Fig. 4. Comparison between OSL and modelled ages. **A:** Plot of the depth in cm of core MD03-2607 versus age in ka showing the extrapolated ages for every cm in the core down to 1500 cm based on the correlation with the global benthic-stack record. Blue circles indicate the 14 tie points used to reconstruct the age model. The red circles and respective error bars represent the ages for the 6 OSL dates calculated in this study. More information is available in Table 1. Note also that the section of the core younger than 40 ka was correlated with radiocarbon dates and other OSL dates already presented in Lopes dos Santos et al. (2012). **B:** Detail for the 55 to 80 ka interval showing the relevant tie points used to produce an age model on which the OSL dates and error bars are juxtaposed. This shows the good age correspondence between the two approaches and that the sedimentation rate was fairly uniform during the 55–80 ka period. (For interpretation of the references to colour in this figure legend, the reader is referred to the Web version of this article.)

3.5. Oceanic fronts

Evidence that the Subantarctic and Polar Fronts (SPF) would have been closer to the core site between 68.6 and 60.8 ka is apparent from shifts towards high percentages of *Turborotalita quinqueloba* and *Neogloboquadrina pachyderma* sinistral, which have been reported today with highest abundances south of the Antarctic Polar Front (Echols and Kennett, 1973; Bé, 1977), as well as in Antarctic waters south of 50°S (in the case of *N. pachyderma* sinistral) for the period of 68.6 to 60.8 ka (Fig. 5C). This phenomenon has similarly been shown for the LGM in the same core (De Deckker et al., 2012). This interpretation is further confirmed by similarly high percentages of *Neogloboquadrina incompta* in the core (Fig. 5C), which seems to thrive above the thermocline (upper 250/200 m of the water column) and can live in the chlorophyll-a maximum zone (Niebler and Gersonde, 1998). During cold phases, this species migrates to shallower water depths and is a good indicator for the Subtropical Front (STF), as shown for the LGM (De Deckker et al., 2012) when percentages were actually lower than for MIS4. Our interpretation is that both oceanic fronts (STF and SPF) would have been very close to one another and close to Australia, especially during the 68.6 to 63.7 ka interval.

3.6. Vegetation record

A number of samples were taken from the 75 to 55 ka interval of the core to determine vegetation composition on land during the time period of interest. An additional three samples were analysed from horizons spanning MIS 5, 3 and 2 for comparative purposes (see Table 2).

To provide information on the most likely source areas for the pollen spectra found in core 2607, statistical analysis was performed on all the pollen spectra and compared with pollen data from the Southeastern Australian Pollen Database (SEAPD) (Kershaw et al., 1994; D'Costa and Kershaw, 1997); see Table 2. The SEAPD was produced using sites studied in southeastern Australia and Tasmania and the pollen assemblages were selected from sample depths that represent the time period immediately before European impact on vegetation. In our study, we excluded all Tasmanian sites and determined the sites within the SEAPD with greatest similarity to the different horizons sampled in the core using unconstrained ordination. Unconstrained ordination was performed on percentage data from 15 of the most common pollen taxa in the SEAPD and in core 2607 in R Core Team (2016) using the non-metric multidimensional scaling routine within the vegan package (Oksanen et al., 2016). The section of the ordination results presented in Fig. 7A focuses on the core 2607 samples and the SEAPD sites with greatest similarity (note that core 2607 level 79.25 ka BP (1000 cm) is not present in this part of the ordination). The geographic location of these 15 SEAPD sites is presented in Fig. 7B.

Using the approach of Cook and van der Kaars (2006), we also developed pollen transfer functions for latitude and annual rainfall. We applied weighted-averaging partial least square regressions to the pollen assemblages from the SEAPD to build the transfer function, and evaluated their predicted ability against modern observational climate data by leave-one-out cross validation. The (leave-one-out) squared correlation between predicted and observed values for latitude, longitude and annual rainfall was 0.59, 0.60 and 0.81 respectively, and (leave-one-out) root mean squared error of prediction for the same functions was 0.56°, 1.61° and 195 mm respectively. The transfer functions were applied to pollen data from the core 2607 sample levels and the results are presented in Table 2. Using the reconstructed latitudes and (Fig. 7B) to provide an indication of likely pollen source area for each level.

We note that for the one sample representing sedimentation during MIS5 [sample taken at 1000 cm in the core and with an age of 79.25 ka], the postulated rainfall was more than twice that of most samples representing MIS4; with the exception of one sample at 60.82 ka, which shows surprisingly high values (see Table 2). Nevertheless, the lowest estimated annual rainfall (366 mm) is found at 65.04 ka. This coincides with the lowest record for percentages of trees and shrubs (see Fig. 5H).

In addition, examination of the percentage of *Sporormiella* spores was also made for all the samples discussed here (Table 2) and it is noteworthy that for the period preceding 55 ka, such spores were always present, thus confirming that megafauna still existed in the Australian landscape. For the three youngest samples (at 43.1, 22.2 and 16.2 ka, see Table 2) spore percentages were

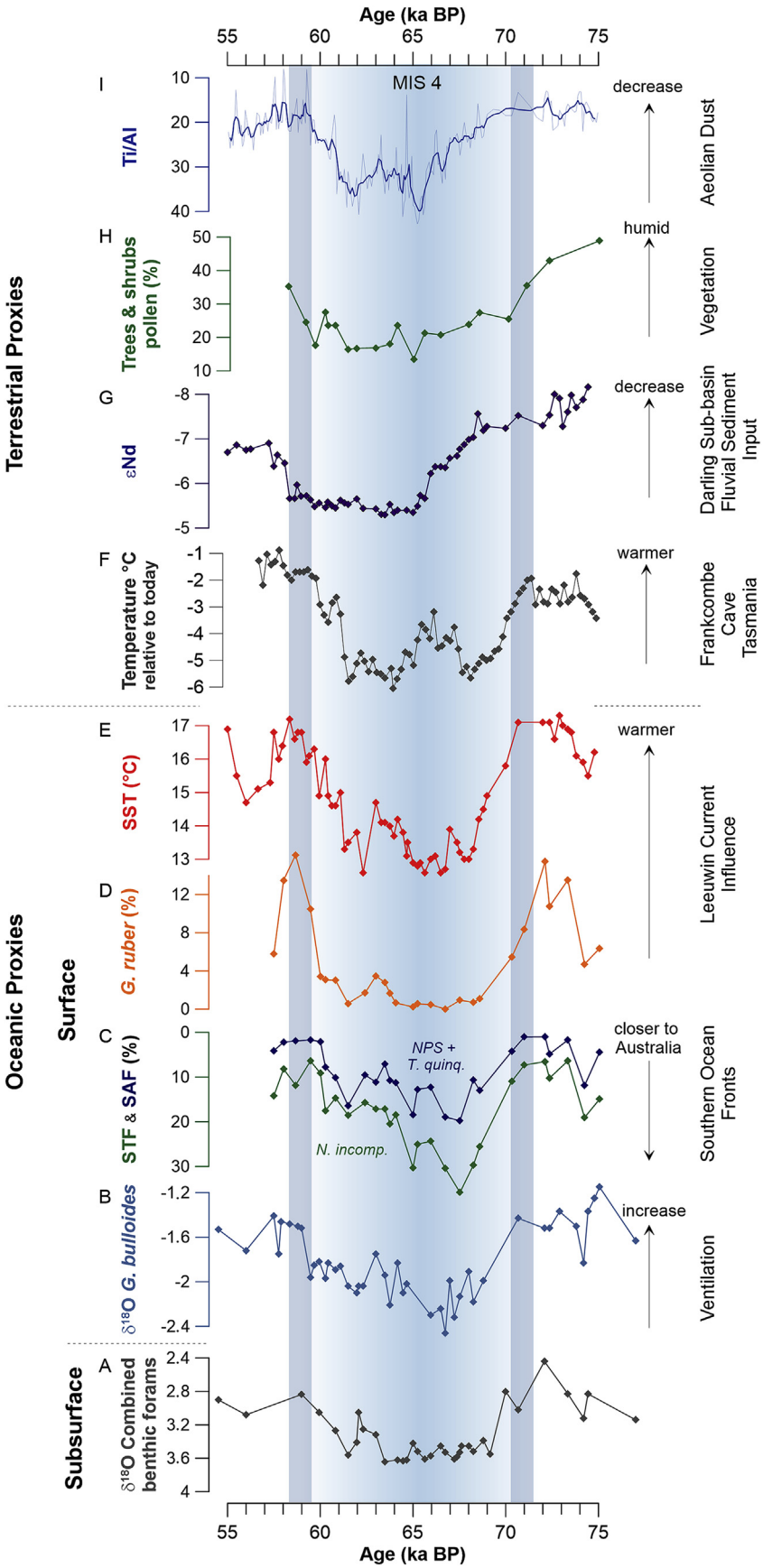

Fig. 5. Selected plots for proxies obtained for core MD03-2607 over the 55 to 75 ka period. **A**: the combined $\delta^{18}O$ record of benthic species, *C. wullerstorfi* and *Uvigerina* species. A value of +0.3‰ was added to the *Uvigerina* samples so as to compensate for the differences between those two genera; **B**: the $\delta^{18}O$ record of the near surface dweller *G. bulloides*; **C**:

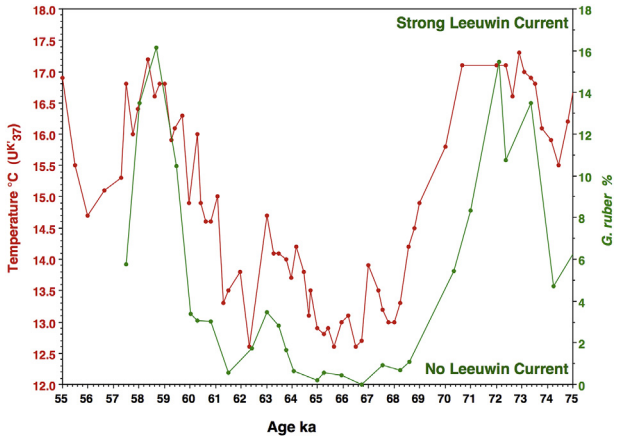

Fig. 6. Comparison of alkenone-reconstructed sea-surface temperatures and percentage counts of the planktic foraminifera *G. ruber*. The presence of this species is indicative of the Leeuwin Current above the MD03-2607 core site.

extremely low, therefore pointing to a lower herbivore biomass; for further explanation, refer to van der Kaars et al. (2017) for a study on a core from offshore Western Australia.

Finally, we also examined the presence of the remains of the ubiquitous alga *Botryococcus* in the samples used for pollen extraction as this alga only grows in non-marine aquatic environments (De Deckker, 1998) and is usually buoyant and therefore can readily be transported to sea. Usually, presence of a large number of such algal cells in marine sediments would indicate the presence of water-borne material, including pollen in a core sample. The low numbers of *Botryococcus* (Table 2) thus suggest that most of the pollen recovered in the core samples were transported aerially.

Pollen spectra for core MD03-2607 show that the total percentage of trees and shrubs relative to herbs, decreased after 72.3 ka (Fig. 5H). This decrease became even more dramatic after 72.3 ka and remained low until 59.7 ka, after which the percentage of trees and shrubs increased again. The lowest percentage of trees and shrubs (13.5%) occurred at 65 ka, and is matched by the highest percentage of herbs (86.5%); a value that is slightly higher than that recorded at 22.2 ka.

We note that the pollen spectra for the interval 75 to 55 ka mimic the vegetation found today in the vicinity of hypersaline Lake Tyrrell (Figs. 1 and 7A-B) in northwestern Victoria, which is a fairly arid region with present-day annual rainfall <400 mm. We do not imply that the pollen found in core 2607 comes from the Lake Tyrrell region.

3.7. Fluvial discharge to the core site: the εNd record

The published record of εNd analyses from core 2607 (Bayon et al., 2017) spanning the time interval of interest has been supplemented with 45 additional analyses to further constrain the discharge of fluvial material to sea during MIS4. These analyses confirm significant discharge of fluvial sediments with a source considered to be from the Darling River catchment (Fig. 1). This area is mostly affected today by summer rains originating from northern Australia. Contrary to the other proxies discussed above, the change

Table 2
List of pollen samples from core MD03-2607 and respective ages used to reconstruct latitude, longitude and past rainfall in mm based on pollen transfer functions discussed in the text.

Depth (cm)	Age (a)	Latitude S	Longitude E	Annual rainfall (mm)	% trees & shrubs	% herbs	*Sporomiella* counts	*Botryococcus* counts
155	16.2	−36.41	142.76	442.2	31.67	68.33	5	25
300	22.2	−36.56	142.06	507.3	15.02	84.98	3	0
560	43.1	−37.07	143.38	698.7	28.72	71.28	1	2
765.5	58.31	−36.51	142.16	491.0	36.26	63.74	22	1
779.5	59.23	−36.33	143.01	429.1	25.66	74.34	28	1
787	59.74	−36.65	142.69	562.8	17.56	82.44	13	1
795	60.28	−36.26	141.59	404.1	27.49	72.51	15	5
797	60.42	−36.72	141.44	460.7	23.58	76.42	12	3
803	60.82	−37.25	142.53	815.7	23.58	76.42	10	1
813	61.5	−36.56	143.02	533.3	16.47	83.53	13	2
817	61.96	−36.16	142.47	415.5	16.70	83.30	16	4
826	63	−36.58	142.61	495.9	16.89	83.11	13	0
837	63.76	−36.27	142.18	467.3	17.99	82.01	15	0
843	64.17	−36.71	142.12	557.8	23.55	76.45	18	2
855.5	65.04	−36.28	142.13	365.6	13.48	86.52	8	0
863	65.63	−36.33	142.60	423.0	21.35	78.65	26	1
874	66.5	−36.43	142.31	415.2	20.75	79.25	21	1
893	68.01	−36.47	141.67	431.7	23.89	76.11	19	0
902.5	68.6	−36.91	142.95	473.1	27.44	71.75	23	2
908.5	70.16	−36.27	142.86	467.9	24.72	75.28	17	1
911.5	71.15	−36.59	142.45	672.5	35.02	64.98	18	1
917	72.36	−36.61	143.12	725.6	42.91	57.09	14	4
947	75.06	−36.47	143.17	557.2	48.90	51.10	14	0
1000	79.25	−37.26	145.81	947.7	52.89	47.11	11	3

percentages of the combination of the subpolar indicator species *N. pachyderma* sin. and *T. quinqueloba* (note the vertical axis is reversed to aid visualisation against other proxies); **D**: percentages of *G. ruber* which is an indicator of the presence of the Leeuwin Current above the core site; **E**: SST estimates based on alkenone thermometry; **F:** plot of temperature relative to today's value in Frankcombe Cave, Tasmania (replotted from Goede et al. (1998); **G**: the εNd record of sediment samples taken from Bayon et al. (2017), supplemented with new data; **H**: percentages of the combination of tree and shrub pollen; **I**: XRF scanning plot of the Ti/Al record from the core [note the vertical axis is reversed]. The thick blue vertical bars represented the approximate boundaries of MIS4 based on all the indicators of change presented in Table 3, using the mean age for the changes and calculated standard deviations. (For interpretation of the references to colour in this figure legend, the reader is referred to the Web version of this article.)

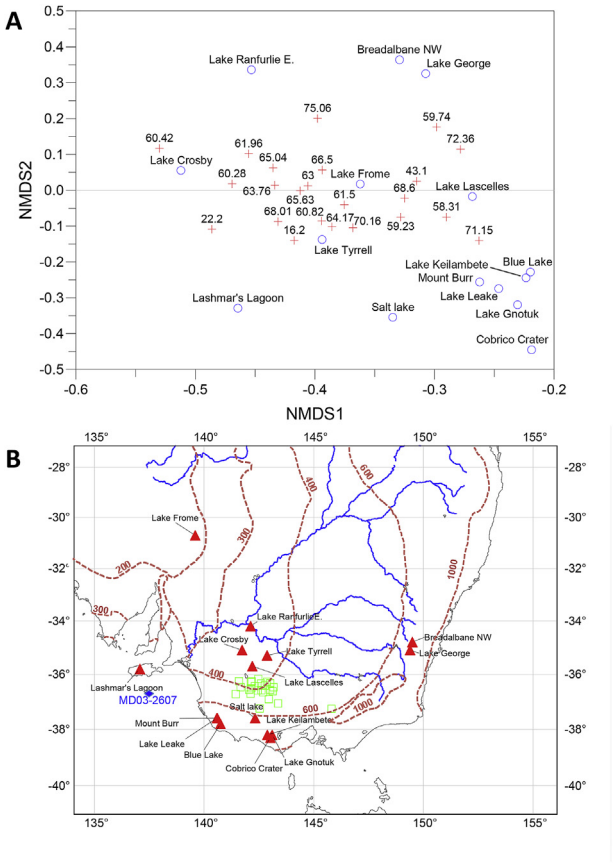

Fig. 7. A: Ordination plot showing sites from the SEAPD (Kershaw et al., 1994; D'Costa and Kershaw, 1997) with greatest affinity to the pollen sample levels from core 2607, please note that sample 82 ka BP (1000 cm) is not present in this part of the ordination. Note that most samples spanning the age range of MIS4 plot in close vicinity with Lake Tyrrell which today occurs in a semi-arid region of Victoria. **B:** Map of SE Australia showing the annual rainfall isohyets taken from the Australian Bureau of Meteorology for the period of 1961–1990. The red triangles show the position of the sites from the SEAPD that had greatest similarity with the pollen samples from core 2607 in unconstrained ordination analysis. The green squares represent the pollen source area for the pollen samples from core 2607 inferred from pollen transfer functions. (refer to Table 2 and text). (For interpretation of the references to colour in this figure legend, the reader is referred to the Web version of this article.)

in εNd signature to less negative values (Fig. 5G) commenced about 72.7 ka, but showed the lowest values during the 65-63.2 ka interval. A return to higher values then continued until 57.3 ka (Fig. 5G).

3.8. Trace metals analyses by XRF core scanning

There are a number of salient features recognized by XRF core scanning, but the most important one relates to the Ti/Al (cps/cps) ratios as an indicator of the supply of airborne material to the core site (see De Deckker et al. (2012) and Stuut et al. (2014)). Starting at 75 ka and continuing until ~70.8 ka, a plateau is visible with ratios ranging between 24 and 13, after which time a progressive increase is noted until 65.3 ka with values remaining high until 60.8 ka. Thereafter, Ti/Al values fluctuate until 59.2 ka, when Ti/Al values retuned to those found before 71 ka (Fig. 5I). Examination of the Ti/Al values for the entire core reveals that during most of the interval spanning MIS4, there was a substantial amount of dust delivered to the core site. Comparison between Fig. 5G and I clearly indicates the lack of concordance between the fluvial discharges at sea shown by the εNd isotopic ratios and the Ti/Al signal, thus indicating that neither Ti nor Al were fluvially transported.

4. Discussion

4.1. MIS4 climate reconstructions across Australasia

Having examined all the proxies obtained from core MD03-2607, we now compare our results with MIS4 conditions reported for the Australian mainland and further afield across the Australasian region (Fig. 8).

4.1.1. Rainfall record for inland Australia

Miller and Fogel (2016) have determined that the average $\delta^{18}O$ in sub-modern emu egg shells is highly correlated with the contemporary point-potential evapotranspiration (PPET) from late austral summer months (February and March) that directly precede egg calcification. Miller et al. (2016) produced an extensive data set of stable oxygen isotopic analyses for flightless emu bird egg shells spanning the period of ~120 to 15 ka. The emu eggshell PPET data in Fig. 8F clearly shows a significant change that commenced soon after 69 ka and which then rapidly changed after 67 ka years, culminating with the highest values being recorded just before 65 ka (Fig. 8F). Soon after that time, PPET values started to decrease and reached a plateau around 60 ka.

We note also that there is a good correlation of discharges from the River Murray to the ocean showing a Darling sub-basin signature as revealed by εNd signatures with PPET values for the Kati Thanda-Lake Eyre basin being at their lowest. This is no surprise as both regions are located at similar latitudes. Thus, central Australia was wet at the peak of MIS4, viz. at 65 ka (see Fig. 9).

4.1.2. Speleothem record from Frankcombe Cave, Tasmania

In southwestern Tasmania, Goede et al. (1998, 1990) examined in great detail a stalagmite that spans MIS4 and that was collected from Frankcombe cave. The chronology of the speleothem is based on four U/Th ages, and disappointingly there is no age for its top which grew during the end of MIS4. Nevertheless, the chronology of the stalagmite record appears satisfactory when comparing its $\delta^{18}O$ data, translated here in temperature departing from today's temperature in the cave (refer to calculations in Goede et al. (1998) and Fig. 5F) and matches well with the chronology of core 2607. It is noteworthy that from ~71.4 ka, temperature decreased rather rapidly in the Tasmanian cave and fell by at least 3.5 °C by 68 ka; this is matched by a SST drop of the same order recorded in core 2607. The discrepancy between the two records, however, is that the low temperature (~4 °C) in the core around 65 ka contrasts with a rise in temperature in the cave of the order of ~2 °C. This remains unexplained but could be the result of a combination of effects such as the source of rainfall in Tasmania combined with cave air temperature.

It is important to mention here that Goede et al. (1998) also examined the Sr isotope composition of the stalagmite spanning MIS4 and identified that the $^{87}Sr/^{86}Sr$ values departed from the composition of the overlying limestone. These authors extrapolated that the higher $^{87}Sr/^{86}Sr$ component during MIS4 likely represents input from terrestrial dust as shown by a greater input of radiogenic Sr dust flux. This scenario is supported by our dust record from core 2607 which reveals higher Ti/Al at the peak of the cold phase of MIS4. Unfortunately, only a few Sr isotope analyses were carried out on the speleothem, which already show two horizons with the highest radiogenic signals at 66.78 ka and 64.8 ka.

4.1.3. Glaciations in Australasia

The set of marine and terrestrial events observed in core 2607 between 75 and 55 ka coincides remarkably well with extensive glaciations in the southern hemisphere. On the South Island of New Zealand, a significant glacial advance has been identified from ^{10}Be

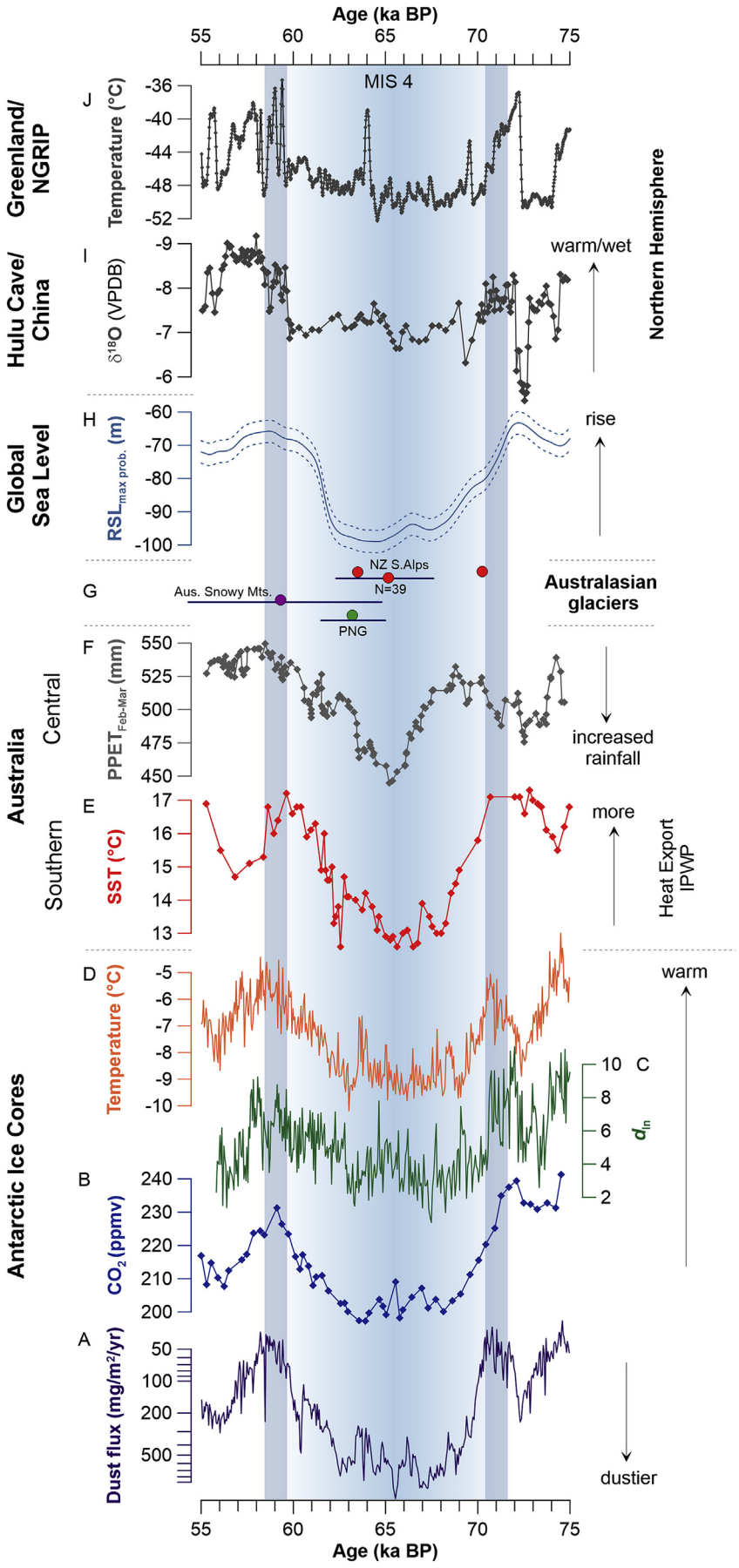
Age (ka BP)
55
60
65
70
75
MIS 4
Greenland/ NGRIP
J
Temperature (°C)
-36
-40
-44
-48
-52
Hulu Cave/ China
I
δ18O (VPDB)
-9
-8
-7
-6
warm/wet
Northern Hemisphere
Global Sea Level
H
RSLmax prob. (m)
-60
-70
-80
-90
-100
rise
NZ S.Alps
N=39
Aus. Snowy Mts.
PNG
G
Australasian glaciers
Australia
Central
F
PPETFeb-Mar (mm)
550
525
500
475
450
increased rainfall
Southern
E
SST (°C)
17
16
15
14
13
more
Heat Export IPWP
Antarctic Ice Cores
D
Temperature (°C)
-5
-6
-7
-8
-9
-10
warm
10 C
8
6
4
2
dln
B
CO2 (ppmv)
240
230
220
210
200
A
Dust flux (mg/m2/yr)
50
100
200
500
dustier
55
60
65
70
75
Age (ka BP)

exposure dating of moraines fringing the modern Lake Pukaki (Schaefer et al., 2015) (Fig. 1). These moraines were deposited between 69 and 61 ka, and have a mean age of 65.1 ± 2.7 ka (see Fig. 8G, red dot). Two other ^{10}Be samples obtained from nearby Lake Tekapo yielded comparable ages of 70.4 and 63.5 ka (see Fig. 8G, red dots with no range provided). These authors concluded from the ^{10}Be chronology that the Balmoral moraines were deposited during MIS4. Of importance here is that the Balmoral moraines extended further down the valleys compared to the younger LGM moraines.

In Papua New Guinea (PNG), a study by Barrows et al. (2001) of the shield volcano Mount Giluwe (Fig. 1), which is located in the country's largest glaciated area, identified four distinct glacial periods, one of which is centred ~62 ka based on ^{36}Cl exposure dating (Komia Glaciation). The critical discovery of this study was that the identified moraines descended further down the slopes of Mount Giluwe compared to the LGM Tongo moraines (Barrows et al., 2011). Unfortunately, only four ages could be obtained for these deposits, with two ages on a single boulder from a terminal moraine indicating deposition at 64.2 ± 11.8 ka. These authors (Barrows et al., 2011) stated that the weighted mean age was 61.9 ± 3.0 ka for the Komia Glaciation (Fig. 8G, green dot).

Geomorphic mapping in the southern highlands of eastern Australia (Snowy Mountains) (Barrows et al., 2001) (Fig. 1) has identified a single glacial advance called the Snowy River Advance, which took place before 59.3 ± 5.4 ka based on (minimum age) ^{10}Be exposure dating of boulders from the BL-I moraine (Fig. 7G, mauve dot). In fact, three ages were obtained as part of this study: 56.0 ± 5.7, 61.7 ± 7.1 and 61.5 ± 6.4 ka (Fig. 8G). The Snowy River Advance was nevertheless more extensive than the younger glaciation.

4.2. Global climate signals for MIS4

4.2.1. The global sea level curve

Other global signals need to be compared with the regional-scale MIS4 reconstructions discussed above, not least because the time period between 75 and 55 ka saw significant and rapid sea level changes. The maximum probability relative sea level (RSL) curve of Grant et al. (2012), plotted in Fig. 7H, shows a drop commencing soon after 72 ka, followed by a much more rapid decline just before 71 ka until ~70.3 ka. After that time, RSL continued to decline at a slower rate and eventually reached a plateau just before 68 ka. This plateau, which lasted for more than a millennium, was followed by an additional RSL drop again to a depth of - 98 m at 64.2 ka. Subsequently, RSL started to rise at a rate of ~6.4 cm/y. Based on Grant et al. (2012)'s data, RSL (maximum probability) first reached a plateau slightly after 59.7 ka, and was followed by a gentle rise at ~58.4 ka.

Overall, based on the above observations, the dramatic MIS4 period commenced 'in full force' when sea level registered a rapid drop at 70.3 ka (Table 3). After the RSL low-stand at 64.8 ka, a rapid rise is noticeable from 62.2 ka to 59.7 ka, followed by a more subtle rise until 59 ka, which likely signified the end of MIS4.

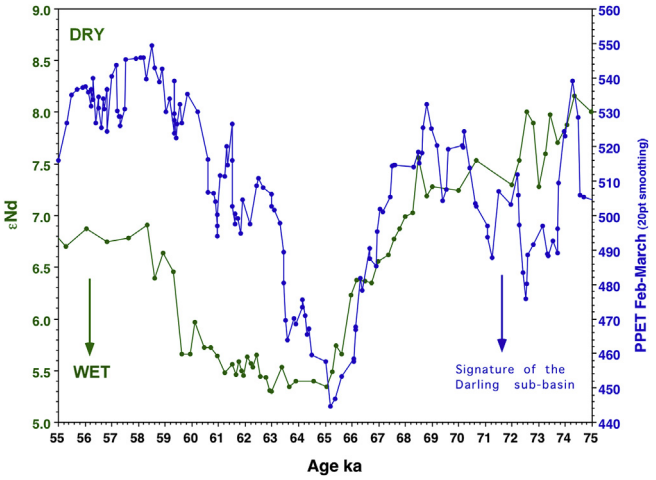

Fig. 9. Comparative plots of εNd data obtained from the core sediments and reconstructed PPET from the Kati Thanda-Lake Eyre basin in central Australia. The less negative εNd values imply discharges to the ocean of sediments from the Darling sub-basin (Bayon et al., 2017) and the lowest PPET values imply high rainfall in central Australia (Miller et al., 2016).

4.2.2. The speleothem record of Hulu Cave, China

The high-resolution and well-dated calcite speleothem δ^{18}O record from Hulu Cave (Wang et al., 2001) (Fig. 1), located close to Nanjing (at 32°30'N), is particularly important for global comparisons of the 75 to 55 ka time period (speleothem MSL). The δ^{18}O record results from a combination of summer monsoon (June to September) rains, which today contribute 80% of the annual precipitation; the rest is contributed during the winter monsoon and it has a heavier δ^{18}O signal (Wang et al., 2001). For the period of interest here (75-55 ka; Fig. 8I), the speleothem record displays a lower contribution of the summer monsoon rains, implying lower transportation of moisture and heat from north of Australia across the Indo-Pacific Warm Pool (De Deckker, 2016).

4.2.3. The MIS4 cryosphere record

When comparing the MIS4 cryosphere record with the MD03-2607 marine record, we focus on the detailed deuterium record (δD_{ice}) of the EPDC core, which has been translated into Antarctic surface temperatures (Jouzel et al., 2007). Here, we concentrate on the 75 to 55 ka record, which is displayed in Fig. 8D. The δD_{ice} record is characterised by a temperature drop and subsequent rise occurring over the period of ~70.6 to 58.5 ka, and a temperature shift of some 4.5 °C; this broadly coincides with the MIS4 interval recorded in core MD03-2607.

Uemura et al. (2012) documented that, for the deuterium excess (d), there is a clear dependency between the modern atmospheric vapor above the Southern Ocean and the relative humidity at the moisture source. Furthermore, a new parameter was defined by Uemura et al. (2012) as the logarithmic definition of deuterium excess d_{ln}, which can be used to identify changes occurring in the

Fig. 8. Selected plots of regional and global proxies related to MIS4 shown over the age interval of 55–75 ka. **A**: the dust flux record from the EPICA Dome C ice core (see Lambert et al., 2008). **B:** combined CO_2 record from the Talos Dome and EPICA EDML ice cores**; C:** deuterium excess record from the EPICA Dome C ice core; **D:** temperature record from the EPICA Dome C ice core; **E**: SST estimates based on alkenone thermometry; **F:** Point-potential evapotranspiration (PPET) in mm from the late austral summer months (February and March) reconstructed for the Kati Thanda-Lake Eyre region of central Australia. Note the reversed axis used here for better visualisation of the results and the use of 20 point smoothing like done in Miller et al. (2016); **G:** Cosmogenic exposure ages of glacial deposits in descending order for the Snowy River Advance on the Kosciuszko Massif (mauve dot, 4 ages), the Komia Glaciation on Mount Giluwe in Papua New Guinea (green dot, 4 ages) and the Balmoral moraine (8) (red dot with error bars for 39 boulder ages around Lake Pukaki, plus 2 other ages at the nearby Lake Tekapo) on the South Island of New Zealand; **H**: Maximum probability of the relative sea level curve (RSL) showing also the 2 standard error range represented by the pale blue envelope; **I:** the δ^{18}O record of a combination of several calcite speleothems from Hulu Cave near Nanjing in China which indicates a low contribution of summer monsoon moisture during MIS4; **J:** the temperature record from the Greenland NGRIP ice core. The thick blue vertical bars represented the approximate boundaries of MIS4 based on all the indicators of change presented in Table 3, using the mean age for the changes and calculated standard deviations. (For interpretation of the references to colour in this figure legend, the reader is referred to the Web version of this article.)

Table 3
Composite list of all the information concerning MIS4 obtained using all the proxies discussed in this paper, showing also in three separate columns (1) the start of MIS4, (2) its termination and (3) the timing of the peak of conditions for that stage. At the bottom, the age range for those three 'events' are provided. The proxies are grouped for those concerning global signals, those for the Australian region, and those from outside Australia. Simple calculations establishing the mean ages and standard deviations for those 3 steps are provided in the right hand table.

Proxi	Start of MIS4 (ka)	Reason for start	End of MIS4 (ka)	Reason for end	MIS4 in full swing (ka)	Reason for full swing	Number of data points covering the 75-55 ka interval [brackets: the 59–71 ka interval]	**Compilaton of global and Australasian signals**				
								Start MIS4	Start MIS4 alternative	End of MIS4	MIS4 in full swing	MIS4 in full swing alternative
Global signals												
Global sea level	**71.8**	start of S/L drop	**59**	end of S/L rise	**64.8**	lowest sea level	**156 (96)**	**71.8**	**71.8**	**59**	**64.8**	**64.8**
Temperature EPICA	**70.5**	temperature starts to drop	**59.3**	temperature high again	**~66.2**	lowest temperature	**377 (214)**	**70.5**	**70.5**	**59.3**	**66.2**	**~66.2**
CO_2 (combining TALDICE & EDML)	**71**	CO_2 drop clearly set	**59.2**	CO_2 high again	**~64**	lowest value	**53 (33)**	**71**	**71**	**59.2**	**64**	**~64**
CH_4 EPICA	**71.2**	CH_4 increases by > 40 ppbv after low at 71.4 ka	**59.1**	CH_4 rapid increase	**?**		**73 (41)**	**71.2**	**71.2**	**59.1**	**65.5**	**65.5**
Dust flux EPICA	**70.4**	dust flux starts to increase	**58.6**	low dust flux	**65.5**	highest dust flux value	**376 (214)**	**70.4**	**70.4**	**58.6**	**64.6**	**63.5**
Deuterium d_{ln} EDC	**70.8**	rapid change synchronous with SST drop	**59**	return to value similar to before MIS4 started	**66**	lowest values encountered	**360 (212)**	**70.8**	**70.8**	**59**	**66**	**66**
Temperature NGRIP	**72.1**	temperature about to drop	**59.6**	peak of temperature rise	**64.6**	lowest temperature encountered	**991 (653)**	**72.1**	**72.1**	**59.6**	**64.6**	**64.6**
Australia												
Benthic forams signal	**70 or 72**	$\delta^{18}O$ values started to become heavier	**59**	$\delta^{18}O$ increased again but low resolution	**64.6 or ~63.5**	heaviest $\delta^{18}O$ values recorded	**232 (29)**	**70**	**72**	**59**	**64.5**	**63.5**
Planktic forams signal	**70.8**	$\delta^{18}O$ values started to become heavier	**60.5**	commencement of lighter values, but full decrease just after 57 ka	**66.8**	heaviest $\delta^{18}O$ value recorded	**42 (29)**	**70.8**	**70.8**	**60.5**	**66.8**	**66.8**
Sea-surface temperature	**70.6**	start of SST drop	**58.4**	SST rising again	**65.6**	lowest SST	**65 (45)**	**70.6**	**70.6**	**58.4**	**65.6**	**65.6**
Leeuwin Current	**72.1**	LC almost absent, but could be a bit earlier due to low resolution	**59.5**	LC in full operation after 58 ka, but low resolution sampling	**67.5 and 64.2**	LC absent (67.5 ka) or near absent (64.2 ka) but insufficient samples	**27 (18)**	**72.1**	**72.1**	**59.5**	**67.5**	**64.2**
Subpolar Front close to core site	**70.3**	SPF foram % starts to increase	**59.5**	SPF foram % starts to decrease but SPF taxa almost absent at 57.3 ka	**~68.7**	highest SPF foram %	**26 (17)**	**70.3**	**70.3**	**59.5**	**68.7**	**68.7**
Pollen spectra	**72.3**	drop of trees & shrubs pollen %	**58.3**	increase of trees & shrubs pollen %	**65**		**20 (18)**	**72.3**	**72.3**	**58.3**	**65**	**65**
Dust Ti/Al	**70.8**	signal starts to increase	**59.2**	Ti/Al values back to pre-MIS4 values	**65.2**	peak of dust deposition	**240 (156)**	**70.8**	**70.8**	**59.2**	**65.2**	**65.2**
eNd river discharge	**~72.7 or 68.6**	Darling sub-basin signature noticeable	**57.35**	Darling sub-basin signature disappears, with change starting at ~59 ka	**63.5**		**61 (50)**	**72.7**	**68.6**	**57.35**	**63.5**	**63.5**
PPET central Australia	**71**	wetness starts to increase	**60 or 58.7**	back to dry conditions	**65.2**	maximum wetness reached	**151 (89)**	**71**	**71**	**60**	**65.2**	**65.2**

(*continued on next page*)

Table 3 (*continued*)

Proxi	Start of MIS4 (ka)	Reason for start	End of MIS4 (ka)	Reason for end	MIS4 in full swing (ka)	Reason for full swing	Number of data points covering the 75–55 ka interval [brackets: the 59–71 ka interval]	**Compilaton of global and Australasian signals**				
								Start MIS4	Start MIS4 alternative	End of MIS4	MIS4 in full swing	MIS4 in full swing alternative
Outside Australia												
New Zealand glaciers	**? 70.4**	one date for Balmoral moraine			**65.1 ± 2.7**	peak of glaciation, but 2 dates for Balmoral moraines at 70.4 ka and 63.5 ka	**39 + 3 + 2**	**70.4**	**70.4**			
Hulu Cave China	**70.1**	start of precipitation change	**59.8–58.6**	shift in precipitation			**145 (60)**	**70.1**	**70.1**	**59.8**		
Additional data on glaciations												
Kosciuszko Massif, Australia			**? 59.3 ± 5.4**	only 1 date			**4 (4)**	**SUMMARY**				
Mt Giluwe, PNG			**61.9 ± 3.0**	4 dates (2 on single boulder; see text)			**4 (4)**	Start MIS4	Start MIS4 alternative	End of MIS4	MIS4 in full swing	MIS4 in full swing alternative
								71.1	**70.9**	**59.1**	**65.5**	**65.2**
								0.8	**0.9**	**0.7**	**1.3**	**1.4**
								18	**18**	**17**	**16**	**16**
												Mean
												St. Dev.
												Number

oceanic moisture-source areas through time when examining the d_{ln} of ice cores. Assuming a fixed location of the moisture source, a higher d_{ln} value would suggest lower humidity and/or higher SSTs over the oceanic moisture source, and vice versa. Considering changes in the spatial distribution of moisture sources, higher d_{ln} values can be interpreted as a larger equatorward shift (i.e., higher SST and lower humidity) of the mean moisture source for Antarctic precipitation (Markle et al., 2016). We have applied this concept with results shown in Fig. 8C and compared the EPICA dome C *d* data (Stenni et al., 2010) against our SST record for core MD03-2607 (Fig. 8E) which shows much greater variations and amplitudes than previously postulated (Markle et al., 2016; Bereiter et al., 2012) from sediment cores for the Southern Hemisphere. Our plot of SST versus d_{ln} for the MD03-2607 core record (Fig. 10) for which we used the revised Antarctic ice core chronology (AICC2012) of Veres et al. (2013) and this shows several notable features: (1) for the period preceding the onset of MIS4, SSTs were high (~17 °C) and, despite significant fluctuations in d_{ln}, indicated lower humidity in atmospheric vapor-source oceans; (2) as soon as SST dropped dramatically, d_{ln} values decreased (Fig. 10) and remained low with some fluctuations, until they eventually started to rise after 63 ka; (3) the rapid rise in SST only started just before 61 ka and continued until the end of MIS4.

The CO_2 record from Antarctic ice cores presented in Fig. 7B shows a gradual reduction after 72 ka, followed by a major drop from 71 ka onwards. The drop continued steadily until 68 ka and then fluctuated until 63.9 ka, before progressively rising until 59.2 ka. After that time, CO_2 values dropped again. The difference in CO_2 values between 71 ka and 64 ka is close to 26 ppmv, but it is interesting to note that the lowest CO_2 value around 64 ka – depending on the record consulted (see supplementary data in Bereiter et al., 2012) – of ~197 ppmv is only slightly higher than for the LGM. During that latter period, CO_2 fluctuated between 184 and 192 ppmv; this would suggest that such low CO_2 values were typically related to full glacial conditions.

Lambert et al. (2008) provide a high-resolution dust flux record for the EPICA core (Fig. 8A), which, for the interval of interest here, clearly mirrors the temperature curve from the same core (Fig. 8D). The highest flux coincides with the lowest temperature trends recorded in core MD03-2607, as shown in Fig. 8E.

In the Northern Hemisphere, the temperature record obtained for the North Greenland Ice Core Project (NGRIP) (Kindler et al., 2014) is presented in Fig. 8J and shows a number of noteworthy features. After Greenland Interstadial 19 (GI19) peaked just before

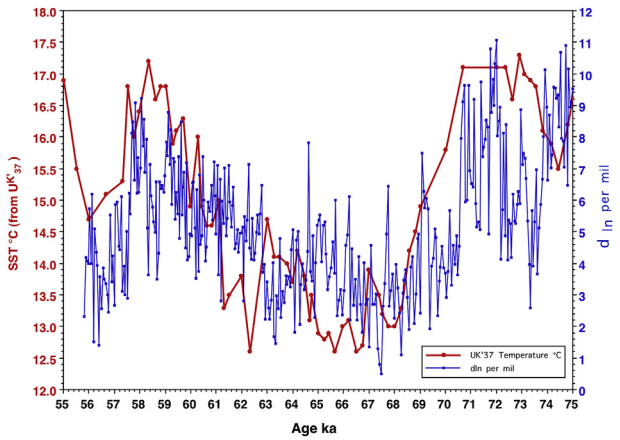

Fig. 10. Plot of the high-resolution of logarithmic definition of deuterium excess d_{ln} (*sensu* Uemura et al., 2012) at EPICA Dome C compared with the low-resolution sea-surface temperature data for core MD03-2607 versus time for the 75 to 55 ka period.

72 ka, a two-stage drop of temperature occurred, and by 69.8 ka temperatures had dropped by 14 °C. It is during this time period that sea level also dropped significantly (Fig. 8H). Temperatures further dropped in Greenland soon after 65 ka, but then rose rapidly by 13.5 °C within 1 ka (= GI18, and corresponding warming event is also seen at EDC (Fig. 8D)), which is likely controlled by the bipolar see-saw mechanism (WAIS Divide Project Members, 2015). Soon after the termination of GI18, cold temperatures resumed and it is not until 59.6 ka (GI17) that temperatures had risen again (Fig. 8J). The global sea level rise, however, had commenced much earlier ~62 ka. It is interesting to note that the lowest NGRIP temperature was reached at 64.5 ka, a little after the maximum cold event in the Southern Hemisphere (see SST in Fig. 8E, peak glaciation in New Zealand in Fig. 8G and dust flux peak in Fig. 8A).

Already, during Greenland cold stadials (WAIS Divide Project Members, 2015), a southward shift of the marine Intertropical Convergence Zone in the northern hemisphere had occurred. This shift is likely to have extended into the tropical region south of the equator, and therefore would have brought enhanced moisture to the region during MIS4 (Chiang et al., 2005). This would, in turn, have generated the supply of moisture that allowed MIS4 glaciers in Australasia discussed here to be more extensive than at the LGM.

4.2.4. Glaciations elsewhere in the southern hemisphere

For the Southern Hemisphere, there is potential evidence of a MIS4 glaciation in Ecuadoran Andes, as mentioned in Clapperton (1990), and the Venezuelan Andes (Kalm and Mahaney, 2011). In New Zealand, prior to the significant work of Schaefer et al., 2015), an Early Otira Glaciation on the west coast of the South Island that extended further down the valleys than during MIS2 had already been identified by McCarthy et al. (2008).

4.3. Other palaeoceanographic records from the southern hemisphere

4.3.1. Sea ice extent in the southern hemisphere

Gersonde and Zielinski (2000) examined the extent of sea ice adjacent to the Antarctic Peninsula and extending further east using a N–S transect of deep-sea cores in the eastern Atlantic and western Indian Ocean sectors. These authors (Gersonde and Zielinski, 2000) used the >3% abundance of siliceous diatoms (*Fragilariopsis curta* and *F. cylindrus*) as sea-ice indicators in sediments, in addition to the presence of the diatom *Fragilariopsis obliquecostata* which is indicative of year-round sea ice influence (sensu Gersonde and Zielinski, 2000). Their study showed that areas of the Antarctic zone that are seasonally covered by sea ice today (3 cores spanning 55°27′S to 53° 58′S), as well the sea ice free Antarctic and Polar Front zones (also today, 52°55′S to 49°S), were, during MIS 4 and 2, predominantly covered by sea ice and seasonally covered by sea-ice, respectively (see Fig. 12 in Gersonde and Zielinski, 2000). In addition, it appears that the percentages of these diatoms were nearly always higher during MIS4 compared to MIS2, thus indicating more extensive sea ice during MIS4. Unfortunately, it was not possible to establish a stable isotope chronology for the cores, hence other methods were used (Gersonde and Zielinski, 2000) and the timing of individual events could not be adequately resolved.

Crosta et al. (2004) studied the diatom content of core SO136-111 located just below the Maximum Winter Sea Ice edge for the Late Holocene (56°40′S, 160°14'E at a water depth of 3912 m). They estimated that sea ice durations during MIS 4 ranged between 1.5 and 0.5 month per year, whereas later they reached up to 2 months per year from 30 ka until the peak of MIS2 at 20 ka. Re-examination of the data for this core by Ferry et al., (2015) concluded that no summer sea ice reached the core site over the last 220 ka, thus reinforcing Crosta et al.'s (2004) finding.

4.3.2. Oceanic changes in the Pacific and Atlantic Oceans

Kaiser et al. (2005) examined ODP core 1233 taken in the southeast Pacific Ocean offshore southern Chile at 41°S which is located below the northbound Peru-Chile Current that originates from Antarctic Circumpolar Current. These authors provide a high-resolution SST data set based on alkenone palaeothermometry for the period 69.2 ka until almost the present. The chronology of the core is radiocarbon-dated back to 40.02 cal yBP, with one additional horizon dated by the palaeomagnetic Laschamp Event at 41 ka. There are 6 additional tie points going back to 69.21 ka which represent SST points tuned to the $\delta^{18}O$ curve from the Byrd polar ice core of Blunier and Brook (2001). The SST data from core 1233 are plotted in Fig. 11E and a question mark is shown to convey the suggestion that perhaps the age correlation with the Byrd ice core ought to be revised for the lower part of the record, simply because the SST curve for core 1233 is very similar to the one from core 2607 (Fig. 11D) except for the older portion of the southern Pacific Ocean core. Comparison with the ice core temperature data shown in Fig. 11F gives added confidence to the suggestion that the chronology for core 1233 ought to be revisited. Nevertheless, we note that the amplitude of temperature change in both marine cores is of the same order between the start of MIS 4 and the coolest period of MIS4 reaching a bit more than 5 °C and this applies, which is comparable to that seen for the EDC ice core (Fig. 11F).

On the other side of the globe in the southeastern Atlantic Ocean, core TNO57-21 (located at 41.1°S) was examined by Barker and Diz (2014) who sampled the core every 2 cm. The chronology of the core for the MIS4 period relies on 4 control points linked to Dansgaard-Oeschger events (in each case, the start of D-O 19, 19a, 18 and 17). For this core, Barker and Diz (2014) looked at the percentages of key planktonic foraminifera taxa with the ratios of some helping identifying the position of the Polar Front (determined by the combination of the polar species *Neogloboquadrina pachyderma* (sin) and *Turborotalita quinqueloba*) with respect to the core site. At the onset of MIS4, an abrupt cooling caused by a significant increase in polar species (Fig. 11A) was noted. Barker and Diz (2014) also commented on the fact that the early stage of MIS4 may have been colder than during MIS2. These authors also noted that mountain glaciers extended further down valley during MIS4 than MIS2 as documented by Denton et al. (1999). This is reiterated by Kaiser et al. (2005) for their findings offshore southern Chile (see discussion above). The timing of the return of the Polar Front in the SE Atlantic seems to have been accomplished earlier than for the frontal shifts south of Australia (Fig. 11A), but this may reflect an insufficiently controlled age model in core TNO57-21. In addition, comparison of the data concerning the position of the fronts recorded in 2607 (Fig. 11B) with that found in the SE Atlantic (Fig. 11A) reveals a similarities in the nature and timing of both data sets.

4.4. Continental environmental conditions in the northern hemisphere

Although it can be difficult to precisely date lacustrine cores and continental sedimentary archives beyond the radiocarbon timescale, there is now ample chronological information about MIS4 environmental changes across multiple continents. Palaeoecological reconstructions for central and northern Europe show the prevalence of dry lakes and a clear shift towards glacial conditions during MIS4 (refer to Fig. 8 in Helmens, 2014). Steppe and arid conditions prevailed for the entire MIS4 period at La Grande Pile in the Vosges, France (Woillard, 1978) and these changes were paralleled by a distinct minimum in mean annual temperatures

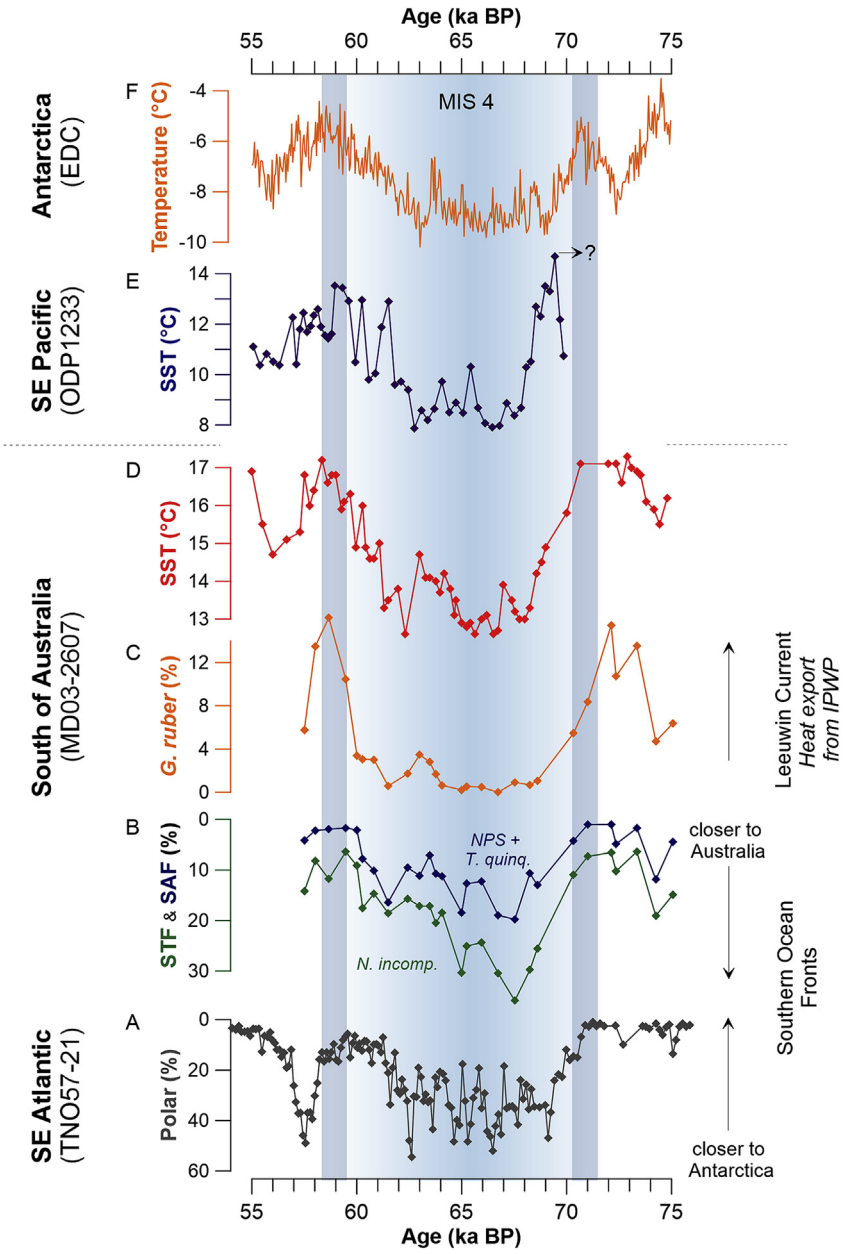

Fig. 11. Selected plots for proxies obtained for various cores and for comparison with core 2607. **A**: percentage of polar species recorded in the SE Atlantic TN057-21 core showing that, when % were high, the polar front was close to the core site; **B**: percentages of the combination of the subpolar indicator species *N. pachyderma* sin. and *T. quinqueloba* (note the vertical axis is reversed to aid visualisation against other proxies) in core 2607; **C**: percentages of *G. ruber* which is an indicator of the presence of the Leeuwin Current above the 2607 core site; **D**: SST estimates based on alkenone thermometry from core 2607; **E:** SST estimates based on alkenone thermometry for SE Pacific Ocean core ODP1233. The question mark points to our suggestion that the chronology of this core ought to be queried (see text for more information); **F**: temperature record from the EPICA Dome C ice core.

(Guiot et al., 1993). In southern Europe, the fen-peat site of Tenaghi Philippon in the intramontane Drama Basin of Eastern Macedonia, Greece, displayed a dominance of steppe herbal taxa after MIS5. The MIS4 percentages of herbal taxa at this site were slightly higher than during MIS2 (Stockhecke et al., 2016), but the total tree percentages were as low as during MIS2, indicating severe arid conditions during MIS4. Further to the southeast, at Lake Van in Turkey (Stockhecke et al., 2016), lake levels were very low during MIS4 due to significantly reduced summer and winter precipitation engendered by a broad atmospheric low that extended from NE Africa to the NE of the Caspian Sea (Fig. 10C in Stockhecke et al., 2016).

4.5. Continental environmental conditions in central Africa

In central Africa, recent evidence has shown a dramatic shift to arid conditions during MIS4, as interpreted from the $dD_{wax\text{-}IV}$ (‰) of leaf waxes that had been transported by wind to a deep-sea core site in the Gulf of Aden (Tierney et al., 2017). By converting this ratio to the dD_{vc} (Collins et al., 2013), we can identify a significant shift in C_3/C_4 plant composition and the presence of a broad spectrum of herbs during MIS4. These ecological changes imply a significant major arid phase north of the African equator, which would have posed a significant challenge for human populations living in Africa (see discussion below in section 6).

4.6. Evidence for glaciation in the northern hemisphere

4.6.1. The Greenland ice core record

For the period spanning 75 to 55 ka, we have plotted the $\delta^{18}O$ record of the two Greenland GRIP ice cores (Kindler et al., 2014) (Fig. 8J, note vertical axis is reversed, which is a proxy for temperature). It is clear that the bipolar see-saw (Blunier and Brook, 2001) did operate between the two hemispheres for both the start and end of MIS4. For example, for the period of ~72 to 70 ka, extremely cold temperatures were registered in Greenland whereas the opposite was registered at EPDC (Fig. 8D; (Jouzel et al., 2007)). We note however, that this is when sea level started to drop (Fig. 8H) and when Hulu Cave in China recorded dry conditions (Fig. 8I). Very soon after 70 ka, a significant temperature shift towards very warm conditions occurred in Greenland, matched by wet conditions for a short while at Hulu Cave; both these trends are opposite to those seen in the SST record of our core (Fig. 8E) and to the glacial conditions evident in New Zealand at Lake Tekapo (Balmoral moraine, Fig. 8G, red dot).

Towards the end of MIS4, when conditions improved in the Southern Hemisphere (Fig. 8E for SST, 8D for Antarctic temperature), the GRIP ice cores record show a slight warming after 59.5 ka. However, this amelioration did not last long and cold temperatures returned by 58 ka.

4.6.2. Glaciations in the northern hemisphere

For the Northern Hemisphere, Lambeck et al. (2010) summarized the extent of maximum glaciation in Scandinavia, when ice coverage peaked at ~ 64 ka with the Karmøy glaciation in Norway, the Ristinge and Old Baltic Ice Advance of Denmark, the Göteborg I in Sweden and the Vuoddasjarvi in Finland. Further, it was pointed out that the glaciation spanning MIS4/3 (~60-55 ka) extended over all of southern Norway (Mangerud et al., 2011), with the adjacent shelves also being ice covered. However, their map of maximum glaciation extent (Fig. 22.5 in Mangerud et al., 2011) indicates that the LGM glaciation (28-20 ka) was slightly more extensive than during MIS4/3. In the North Sea Basin, Graham et al. (2011) discussed what they refer to as the 'Early Weichselian Glaciation' for the Norwegian Channel and Atlantic margin and from the northern North Sea area. They report that these regions saw extensive grounded MIS4 ice sheets, and implied significant ice cover in the North Sea area. Unfortunately, they did not compare the extent of the MIS4 and LGM ice sheet extents in this region. In addition, there is evidence that, during the ~65–60 ka period, the Scandinavian and British Ice Sheets merged during the Sundsøre ice advance from the north into Denmark and the North Sea (Larsen et al., 2009). In Japan, in the Hidaka Mountains of Hokkaido Island, (Sawagaki and Aoki (2011) identified a 'maximum glacial extension … that occurred before the LGM and probably during MIS4'. These authors also briefly point out more extensive glaciation during MIS4 compared to MIS2 in Taiwan. It is necessary to point out that all of these references to MIS4 glaciations have relied on poor chronological control, although they have been able to show that the glacial features of interest are much older than those generated during the LGM.

4.7. The effect of solar insolation during MIS4

Examination of the insolation data provided by Berger and Loutre (1991) for two selected latitudes (65°N and 15°N) and for the mid-month of July clearly identifies that, at 70 ka, insolation had reached a minimum value of 407 Watt/m^2 at 65°N and of 434 Watt/m^2 at 15°N, and that values close to these minima were sustained for at least 2 millennia either side of 70 ka (Fig. 12). It is no surprise therefore to see that the start of MIS4 coincides with this period assuming a substantial glacial advance in at least the Northern Hemisphere, which, as a consequence, would have engendered a significant sea level drop (Fig. 8H). Nevertheless, it is important to note that RSL (Grant et al., 2012) had started to recede just after 71.8 ka. Based on insolation data for the Northern Hemisphere - assuming that the ice sheets there had the greatest influence on sea level changes - the termination of MIS 4 is seen at 59 ka, but the return to higher insolation values reached a plateau around 57-55 ka at 65°N. Global sea level had already become shallower well before that period, and were close to 66 m at ~58.5 ka (Fig. 8H).

5. Towards a better definition of MIS4 in the Australasian region

Examination of all the proxies from core 2607 clearly indicates that significant changes occurred in a series of steps in the Australian region during MIS4. These consist of:

1. The early record:
   a. Soon after 72 ka, the Leeuwin Current (LC) began losing influence over the core site (Fig. 5D) and this is paralleled by a shift in oceanic fronts, as indicated by an increase in the percentage of foraminifer indicator species for the Subpolar Front at the core site (Fig. 5C);
   b. There is a rapid shift towards heavier $\delta^{18}O$ benthic isotope values soon after 72 ka (Fig. 5A) as a result of a global sea level drop, which in turn coincides with a rapid drop in SST (Fig. 8E). At the same time (although sample resolution is low), there is significant vegetation change in southeastern Australia, with the % of trees and shrubs starting to drop (Fig. 5H) and the % of herbs increasing; arid conditions have begun on land at the time when sea temperatures drop, and the dust signal increases in the core record (Fig. 5I).
   c. During MIS4, a very large temperature drop (~5 °C) was registered in core 2607 as well as in Frankcombe Cave in Tasmania, although the maximum temperature drop found in both records did not coincide. A similar temperature drop with the same amplitude was registered in the southeastern portion of the Pacific Ocean in ODP core 1233. Equally, cold (polar) oceanic fronts shifted northward offshore South Australia and in the southeastern Atlantic Ocean.

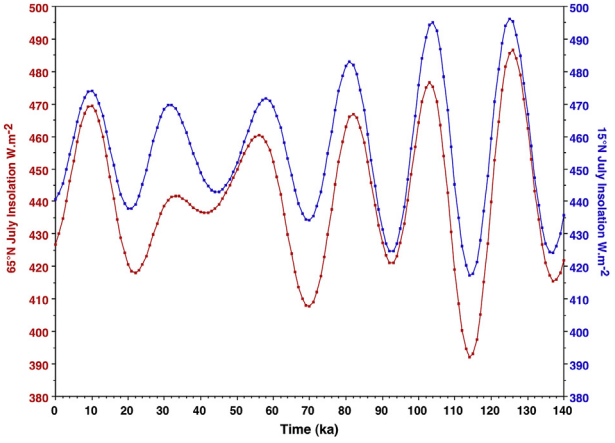

Fig. 12. Plot of the mid-month insolation data in Watt/m^2 obtained from Berger and Loutre (1991) spanning the period of 0–140 ka, for July for 65°N and 15°S. The original insolation values are in langleys/day (cal/cm^2/day), multiplied by 0.4843 to convert to Watts/m^2.

d. The εNd record indicates that the Murray-Darling system (Fig. 5G) was still receiving water in its northern sector, as the sediment delivered to sea at the core site bears a Darling sub-basin signature; this is confirmed by a temporary increase in the point-potential evapotranspiration (PPET) from the late austral summer months (February and March) for the Kati Thanda-Lake Eyre region of central Australia (Figs. 8F and 9).
2. The culmination of changes at sea and on land occurred around 65.5 ka, ignoring the evidence of the Subpolar Front indicator species (Fig. 5C), which show a slightly earlier peak shift (~67.5 ka). At that time, SST were at their lowest, the LC was absent, trees and shrub vegetation cover was much reduced, and the delivery of airborne dust at sea was at its maximum. Nevertheless, in central Australia, the PPET late austral summer moisture had peaked (Fig. 8F) and this is paralleled with a very high discharge of Sub-Darling basin fluvial sediments (Fig. 5G).
3. By 59 ka conditions progressively returned to those seen before the sea level and SST drop. We nevertheless observe continued improvement in a range of conditions both at sea and on land continued after 59 ka.

Finally, comparison of *G. ruber* % with the SST data obtained from alkenone thermometry from core 2607 (Fig. 5D–E) informs us that a very rapid and significant SST drop after 70.5 ka may have coincided with the sudden disappearance of the Leeuwin Current (LC). This would have implied the presence of westerly winds close to the Australian mainland after 70.6 ka (as envisaged by De Deckker et al. (2012) for the LGM when the LC could not circumnavigate the southern tip of Western Australia), causing dry conditions in the southern part of the Australian continent. This condition was maintained until slightly before 62 ka, once SST began to rise.

The OSL dating study in the Strzelecki and Tirari Deserts of central Australia (Fitzsimmons et al., 2007a,b) indicated that there were distinct periods of enhanced aeolian activity between 73 and 66 ka. It is clear that a dramatic change of conditions occurred after this time period with a marked wetting of central Australia, as discussed in the following section.

We note that the evidence for a large amount of moisture in central Australia (Miller et al., 2016) is supported by the high lake levels of Kati-Thanda-Lake Eyre (Magee et al., 2004) with a pooled mean age of at 64.3 ± 2.5 ka (Phase III has 6 OSL ages pertaining to a lake level of −3 m above the Australian Height datum, compared with today's dry lake floor being at −15m AHD). Later on, Cohen et al. (2015) who used single grains for OSL dating determined that both Lakes Frome & Kati Thanda Eyre registered highstands between 66±3 (L. Frome) and 60±2ka (Kati Thanda-Lake Eyre), which adds further precision to Magee et al. (2004)'s findings. Not only would this monsoon moisture have fed the central Australian region, but it would have extended as far as the highlands of SE Australia to fed the small glacier on the Kosciuszko Massif, and also the Pukaki Glacier on the South Island of New Zealand. On its way to the southern latitudes, this moisture would have also fed the Komia glacier of Mount Kiluwe in Papua New Guinea.

Three of the proxies obtained from Antarctic ice cores, namely temperature (Fig. 8D; Jouzel et al., 2007), CO_2 (Fig. 8B (Bereiter et al., 2012) and deuterium excess – translated here into d_{ln} (see Uemura et al., 2012) - (Fig. 8C) and dust flux (Fig. 8A; Lambert et al., 2008) clearly indicate a dramatic change of conditions occurred around 71 ka, and returned to 'normality' around 59 ka. MIS4 was a significant period with CO_2 levels almost as low as during the LGM. The dust record (Lambert et al., 2008, 2015) implies a 'dusty world', at least in the Southern Hemisphere. The change in deuterium excess d_{ln} indicates higher moisture supply to Antarctica, and is confirmed by a parallel change in SST offshore from southern Australia (Fig. 8E), as well as a change in Australian dust supply to the ocean (Fig. 5I).

However, contrary to all the other proxies in Antarctica cores and those obtained from the 2607 core, sea level rise commenced much earlier at the end of MIS4, starting at ~62 ka and eventually reaching sustained higher levels by 58.2 ka. The early sea level rise implies a change in the Northern Hemisphere, and the likely explanation is the advent of meltwater from decaying northern ice sheets that engendered Heinrich Stadial 6 (HS-6) (for further details refer to Schaefer et al. (2015). It was previously demonstrated that Heinrich stadials coincide with the strength of the Leeuwin Current (De Deckker et al., 2012) which can reach the southern coast of Australia, and that this is facilitated by relaxation of the southern hemisphere westerlies. This typifies the 'bipolar see saw' discussed in De Deckker et al. (2012), which is clearly visible when comparing the Greenland ice core record ($\delta^{18}O$ as a proxy for temperature) displayed in Fig. 8J.

6. Implications for human dispersal

It has previously been suggested that orbitally-forced climatic shifts would have been the drivers of 'Out of Africa' *Homo sapiens* migration (Müller et al., 2011; Timmermann and Friedrich, 2016). Tierney et al. (2017) concluded that the rapid deterioration in climate conditions during MIS4 would have acted as a major 'push' factor in the migration of human populations out of Africa towards Eurasia. Conditions in northern Europe at this time would have been very dry and cold. However, human migration eastwards through Eurasia would have been favoured by global low sea-levels that coincided with MIS4 climatic shifts. The recent discovery that humans had colonized northern Australia by 65 ka ago (Clarkson et al., 2017; see related discussions in Dortch and Malaspinas, 2017; Veth, 2017; Hiscock, 2017; Wood, 2017; Clarkson et al., 2018; O'Connell et al., 2018) reinforces the significance of MIS4 orbital pacing on the 'Great Arc' of modern human dispersal (Fig. 1A in Bae et al., 2017). Humans would have reached Australia at a time of lower sea level and when the region was experiencing cooler and wetter conditions in the northern part of the continent. The latter is borne out by the oxygen-isotope egg shell evidence for a very wet central Australia (Miller et al., 2016), which we interpret as resulting from a southern shift of the ITCZ peaking at 65 ka. The human populations that first reached Australia would have commenced their migration when arid conditions prevailed in Africa. Our marine core record and synthesis of Australasian climate archives suggests humans would have been met with suitable conditions for settlement in northern Australia during MIS4. This is a time when sea levels had dropped by 100 m and northern Australia would have been wet. Bird et al. (2018) have recently argued that when low sea levels would have revealed a series of islands (now submerged) and would have favoured access to people traversing the Timor Sea and likely originating from the Islands of Roti and Timor in southern Wallacea. Norman et al. (2018) have also modelled the possible pathways of human early colonisation into northwest Australia 70-60 ka and this was followed by Bird et al. (2018) who modelled people's movement during a 75 m sea level drop. We argue here that a 100 m sea level drop was even more propitious for human sea faring and migration at 65 ka. Monsoonal activity was weaker as recorded by van der Kaars et al. (2010) during MIS4 in a core located offshore SW Sumatra, but northern Australia would have still been very wet according to the dataset of Miller et al. (2016) which argued for a wet Lake Eyre Basin that is fed waters arising from the north.

7. Conclusion

The period spanning 75 to 55 ka is characterised by dramatic environmental change in the Southern Hemisphere, as evident from the multi-proxy record of marine core MD03-2607 and an array of Australasian palaeoclimate archives spanning the ocean, land, cryosphere and atmosphere. In particular, there was a rapid and steep global sea-level drop at ~71 ka, which is also seen in the benthic foraminifera record. MIS4 had commenced by this time period, and changes in SL were paralleled by a rapid and significant sea-surface temperature drop. The warm Leeuwin Current had vanished along the southern coast of Australia, and the westerlies belt would have come closer to the continent as well as to the subpolar front. Pollen spectra from our marine core also show that the vegetation cover in (southern) Australia adjusted towards more semi-arid conditions. Peaking around 65 ka, sea level had dropped by close to 100 m globally, glacial conditions prevailed, and several regional glaciers were more extensive than during the LGM. Examples of the latter can be seen on the South Island of New Zealand, in Papua New Guinea and in the Snowy Mountains of SE Australia. Such significant advances require an explanation: was it much colder or wetter, or both, at the time of MIS4 to justify more extensive glaciers during MIS4? It appears that a larger supply of moisture may have fed the glaciated regions since we now know that central Australia received a significant amount of moisture in late summer/autumn, as evidenced by the $\delta^{18}O$ record at Hulu Cave in China (Wang et al., 2001) (Fig. 8I). This implies that the Intertropical Convergence Zone during MIS4 would have extended further south over Australia, and this southward shift may have peaked around 65 ka when the Kati Thanda-Lake Eyre region (Fig. 1) was much wetter (Miller et al., 2016).

A compilation of all the ages for the boundaries and peak conditions of MIS4 across the Australasian region and elsewhere is presented in Table 3. Using these chronologies, we define the regional start and end ages of MIS4 as 71 ± 0.8 ka and 59 ± 0.7 ka, respectively, with peak condition occurring around 65.5 ± 1.3 or 65.2 ± 1.4 ka (Table 3, wirh the summary section at the bottom right hand corner).

From our synthesis, it is clear that MIS4 was a significant glacial period that affected the Southern Hemisphere. Similar detailed and well-dated, regional-scale analyses are required for the Northern Hemisphere, but there is significant evidence to suggest that this glacial period, long ignored, ought to be further investigated globally using new state-of-the art dating techniques.

This period, which lasted for 11 millennia (Table 3), would have acted as a significant 'push' and 'pull' catalyst for modern human dispersal out of Africa and across Eurasia, and would have ensured suitable conditions for the human colonisation of northern Australia ~65 ka.

Author contributions

PDD conceived the project and wrote the first draft of the paper to which all authors contributed; LJA performed the OSL measurements and wrote all the methods and supplementary sections on this technique with the help of MD; SvdK counted the palynoflora and reconstructed the terrestrial paleoenvironments; GB performed the Nd isotope analyses; JBS conducted the XRF scans; KP performed the foraminiferal counts; RLdS conducted and interpreted the alkenone analyses; RU helped interpret the deuterium results from the Antarctic ice core.

Conflicts of interest

The authors declare no conflict of interest.

Acknowledgements

PDD is grateful to Yvon Balut who was instrumental in obtaining the core with the CALYPSO corer (designed by him) with the RV Marion Dufresne funded by IPEV. Judith Shelley skillfully prepared foraminifera for isotopic analysis and performed other analyses to support the work on AAR and OSL analyses. Financial support for the OSL dating research was provided by Australian Research Council Future Fellowship project FT130100195 and ARC Discovery Early Career Researcher Award DE160100743. LA thanks A. Zawadzki at ANSTO for performing alpha-particle spectrometry measurements on the OSL dating samples. GB thanks Emmanuel Ponzevera and Alexis De Prunelé at IFREMER for help during Nd isotopic measurements. Larissa Schneider and Janelle Stevenson from the ANU Centre for Biodiversity Analysis processed several samples prior to pollen counting and Martine Hagen processed additional ones at the Sediment Laboratory of the Vrije Universiteit Amsterdam. Michael Gagan kindly allowed for free isotopic analyses on foraminifera from the MIS4 interval that were performed at the Research School of Earth Sciences at ANU by Joan Cowley. PDD is grateful to Drs K. Grant and F. Hibbert for discussions concerning their relative sea level curve and coral depth indicators around MIS4. Barbara Stenni provided the isotope data from EDC. We thank Rineke Gieles for assistance with the XRF scanning at NIOZ, Albert Goede for sharing his oxygen isotope data from Frankcombe Cave and showing some unpublished diagrams from his PhD thesis, and to Professor G. Denton as well as Dr A. Putnam for providing pertinent references that helped improve links with oceanic changes in the Southern Hemisphere with our core data. In addition, our paper benefitted from the pertinent comments of Professor James Shulmeister and another anonymous reviewer.

Appendix A. Supplementary data

Supplementary data to this article can be found online at https://doi.org/10.1016/j.quascirev.2018.11.017. The data used to plot figs 5, 8 and 11 are available at the www.pangaea.de web site.

References

Arnold, L.J., Roberts, R.G., 2009. Stochastic modelling of multi-grain equivalent dose (D_e) distributions: implications for OSL dating of sediment mixtures. Quat. Geochronol. 4, 204–230.

Arnold, L.J., Roberts, R.G., Galbraith, R.F., DeLong, S.B., 2009. A revised burial dose estimation procedure for optical dating of young and modern-age sediments. Quat. Geochronol. 4, 306–325.

Arnold, L.J., Demuro, M., Navazo Ruiz, M., Benito-Calvo, A., Pérez-González, A., 2013. OSL dating of the middle palaeolithic hotel California site, Sierra de Atapuerca, north-central Spain. Boreas 42, 285–305.

Arnold, L.J., Duval, M., Demuro, M., Spooner, N.A., Santonja, M., Pérez-González, A., 2016. OSL dating of individual quartz 'supergrains' from the Ancient Middle Palaeolithic site of Cuesta de la Bajada, Spain. Quat. Geochronol. 36, 78–101.

Aitken, M.J., 1985. Thermoluminescence Dating. Academic Press, London, 359 p.

Barker, S., Diz, P., 2014. Timing of the descent into the last Ice Age determined by the bipolar seesaw. Paleoceanography 29, 489–507. https://doi.org/10.1002/2014PA002623.

Barrows, T.T., Stone, J.O., Fifield, L.K., Cresswell, R.G., 2001. Late Pleistocene glaciation of the Kosciuszko Massif, Snowy mountains, Australia. Quat. Res. 55, 179–189.

Barrows, T.T., Hope, G.H., Prentice, M.L., Fifield, L.K., 2011. Late Pleistocene glaciation of the Mt Giluwe volcano, Papua New Guinea. Quat. Sci. Rev. 30, 2676–2689.

Bayon, G., German, C.R., Boella, R.M., Milton, J.A., Taylor, R.N., Nesbitt, R.W., 2002. Sr and Nd isotope analyses in paleoceanography: the separation of both detrital and Fe–Mn fractions from marine sediments by sequential leaching. Chem. Geol. 187, 179–199.

Bayon, G., Toucanne, S., Skonieczny, C., André, L., Bermell, S., Cheron, S., Dennielou, B., Etoubleau, J., Freslon, N., Gauchery, T., Germain, Y., Jorry, S.J., Ménot, G., Monin, L., Ponzevera, E., Rouget, M.-L., Tachikawa, K., Barrat, J.A., 2015. Rare earth elements and neodymium isotopes in world river sediments revisited. Geochem. Cosmochim. Acta 170, 17–38.

Bayon, G., De Deckker, P., Magee, J.W., Germain, Y., Bermell, S., Tachikawa, K., Norman, M.D., 2017. Extensive wet episodes in Late Glacial Australia resulting

from high-latitude forcings. Science Reports 7, 44054. https://doi.org/10.1038/srep44054.
Bé, A.W.H., 1977. An ecological, zoogeographic and taxonomic review of recent planktonic foraminifera. In: Ramsay, A.T.S. (Ed.), Oceanic Micropaleontology 1. Academic Press, London), pp. 1–100.
Bereiter, B., Lüthi, D., Siegrist, M., Schüpbach, S., Stocker, T.F., Fisher, H., 2012. Mode change of millennial CO_2 variability during the last glacial cycle associated with a bipolar marine carbon seesaw. Proc. Natl. Acad. Sci. 109, 9755–9760.
Berger, A., Loutre, M.F., 1991. Insolation values for the climate of the last 10 million years. Quat. Sci. Rev. 10, 97–317.
Bird, M.I., Beaman, R.J., Condie, S.A., Cooper, A., Ulm, S., Veth, P., 2018. Palaeogeography and voyage modeling indicates early human colonization of Australia was likely from Timor-Roti. Quat. Sci. Rev. 181, 431–439.
Blunier, T., Brook, E.J, E.J., 2001. Timing of millennial-scale climate change in Antarctica and Greenland during the last glacial period. Science 291, 109–112.
Bouvier, A., Vervoort, J.D., Patchett, P.J., 2008. The Lu–Hf and Sm–Nd isotopic composition of CHUR: constraints from unequilibrated chondrites and implications for the bulk composition of terrestrial planets. Earth Planet Sci. Lett. 273, 48–57.
Brennan, B.J., 2003. Beta doses to spherical grains. Radiat. Meas. 37, 299–303.
Chiang, J., Bitz, C., 2005. Influence of high latitude ice cover on the marine Intertropical Convergence Zone. Clim. Dynam. 25, 477–496.
Clapperton, C.M., 1990. Glacial and volcanic geomorphology of the Chimborazo-Carihuairazo Massif, Ecuadoran Andes. Trans. R. Soc. Edinb. Earth Sci. 81, 91–116.
Clarkson, C., Jacobs, Z., Marwick, B., Fullagar, R., Wallis, L., Smith, M., Roberts, R.G., Hayes, E., Lowe, K., Carah, X., Florin, S.A., McNeil, J., Cox, D., Arnold, L.J., Hua, Q., Huntley, J., Brand, H.E.A., Manne, T., Fairbairn, A., Shulmeister, J., Lyle, L., Salinas, M., Page, M., Connell, K., Park, G., Norman, K., Murphy, T., Pardoe, C., 2017. Human occupation of northern Australia by 65,000 years ago. Nature 547, 306–310.
Clarkson, C., Roberts, R.G., Jacobs, Z., Marwick, B., Fullagar, R., Arnold, L.J., Hua, Q., 2018. Reply to comments on Clarkson et al. (2017) 'Human occupation of northern Australia by 65,000 years ago'. Aust. Archaeol. 84, 84–89.
CLIMAP Project Members, 1976. The surface of the ice-age Earth. Science 191, 1131–1137.
Cohen, T.J., Jansen, J.D., Gliganic, L.A., Larsen, J.R., Nansen, G.C., May, J.-H., Jones, Price, D.M., 2015. Hydrological transformation coincided with megafaunal extinction in central Australia. Geology 43, 195–198.
Collins, J.A., Schefuß, E., Mulitza, S., Prange, M., Werner, M., Tharammal, T., Paul, A., Wefer, G., 2013. Estimating the hydrogen isotopic composition of past precipitation using leaf-waxes from western Africa. Quat. Sci. Rev. 6, 88–101.
Cook, E.J., van der Kaars, S., 2006. Development and testing of transfer functions for generating quantitative climatic estimates from Australian pollen data. J. Quat. Sci. 21, 723–733.
Crosta, X., Sturm, A., Armand, L., Pichon, J.-J., 2004. Late Quaternary sea ice history in the Indian sector of the Southern Ocean as recorded by diatom assemblages. Mar. Micropaleontol. 50, 209–223.
D'Costa, D.M., Kershaw, A.P., 1997. An expanded recent pollen database from southeastern Australia and its potential for refinement of palaeoclimatic estimates. Aust. J. Bot. 45, 583–605.
De Deckker, P., 1998. Biological and sedimentary facies of Australian salt lakes. Palaeogeogr. Palaeoclimatol. Palaeoecol. 62, 237–270.
De Deckker, P., 2016. The Indo-Pacific Warm Pool: critical to world oceanography and world climate. Geoscience Letters 3, 20. https://doi.org/10.1186/s40562-016-0054-3.
De Deckker, P., Norman, M., Goodwin, I.D., Wain, A., Gingele, F.X., 2010. Lead isotopic evidence for an Australian source of aeolian dust to Antarctica at times over the last 170,000 years. Palaeogeogr. Palaeoclimatol. Palaeoecol. 285, 205–223.
De Deckker, P., Moros, M., Perner, K., Jansen, E., 2012. Influence of the tropics and southern westerlies on glacial interhemispheric asymmetry. Nat. Geosci. 5, 266–269.
Demuro, M., Arnold, L.J., Froese, D.G., Roberts, R.G., 2013. OSL dating of loess deposits bracketing Sheep Creek tephra beds, northwest Canada: dim and problematic single-grain OSL characteristics and their effect on multi-grain age estimates. Quat. Geochronol. 15, 67–87.
Denton, G.H., Lowell, T.V., Heusser, C.J., Schluchter, C., Andersen, B.G.,, Heusser, L.E., Moreno, P.I., Marchant, D.R., 1999. Geomorphology, stratigraphy, and radiocarbon chronology of Llanquihue drift in the area of the southern lake District, Seno Reloncavi, and Isla Grande de Chiloe, Chile. Geografiska Annaler, Series A 81A (2), 167–229.
Dortch, J., Malaspinas, A.S., 2017. Madjedbebe and genomic histories of Aboriginal Australia. Aust. Archaeol. 83, 174–177.
Echols, R.J., Kennett, J.P., 1973. Distribution of Foraminifera in surface sediments. Antarctic Folio Series 17, 13–17.
Emiliani, C., 1955. Pleistocene temperatures. J. Geol. 63, 538–578.
Ferry, A.J., Crosta, X., Quilty, P.G., Fink, D., Howard, W., Armand, L.K., 2015. First records of winter sea ice concentration in the southwest Pacific sector of the Southern Ocean. Paleoceanography 30, 1525–1539.
Fitzsimmons, K.E., Bowler, J.M., Rhodes, E.J., Magee, J.W., 2007a. Relationships between desert dunes during the late Quaternary in the Lake frome region, Strzelecki Desert, Australia. J. Quat. Sci. 22, 549–558.
Fitzsimmons, K.E., Rhodes, E.J., Magee, J.W., Barrows, T.T., 2007b. The timing of linear dune activity in the Strzelecki and Tirari Deserts, Australia. Quat. Sci. Rev. 26, 2598–2616.
Galbraith, R.F., Roberts, R.G., Laslett, G.M., Yoshida, H., Olley, J.M., 1999. Optical dating of single and multiple grains of quartz from Jinmium rock shelter, northern Australia: Part I, experimental design and statistical models. Archaeometry 41, 339–364.
Gersonde, R., Zielinskim, U, U., 2000. The reconstruction of late Quaternary Antarctic sea-ice distribution—the use of diatoms as a proxy for sea-ice. Palaeogeogr. Palaeoclimatol. Palaeoecol. 162, 263–286.
Gingele, F.X., De Deckker, P., 2004. Fingerprinting Australia's rivers with clay minerals and the application for the marine record of climate change. Aust. J. Earth Sci. 51, 339–348.
Gingele, F.X., De Deckker, P., 2005. Late Quaternary fluctuations of palaeoproductivity in the Murray Canyons area, south Australian continental margin. Palaeogeogr. Palaeoclimatol. Palaeoecol. 220, 361–373.
Gingele, F.X., De Deckker, P., Morman, M., 2007. Late Pleistocene and Holocene climate of SE Australia reconstructed from dust and river loads deposited offshore the River Murray Mouth. Earth Planet Sci. Lett. 255, 257–272.
Goede, A., Veeh, H.H., Ayliffe, L., 1990. Late Quaternary palaeotemperature records for two Tasmanian speleothems. Aust. J. Earth Sci. 37, 267–278.
Goede, A., McCulloch, M., McDermott, F., Hawkesworth, C., 1998. Aeolian contribution to strontium and strontium isotope variations in a Tasmanian speleothem. Chem. Geol. 149, 37–50.
Graham, A.G.C., Stoker, M.S., Lonergan, L., Bradwell, T., Stwart, M.A., 2011. The Pleistocene glaciations of the north Sea Basin. Dev. Quat. Sci. 15, 261–278.
Grant, K.M., et al., 2012. Rapid coupling between ice volume and polar temperature over the last 150,000 years. Nature 491, 744–747.
Guérin, G., Mercier, N., Adamiec, G., 2011. Dose-rate conversion factors: update. Ancient TL 29, 5–8.
Guiot, J., de Beaulieu, J.L., Chedaddi, R., David, F., Ponel, P., Reille, M., 1993. The climate in Western Europe during the last Glacial/Interglacial cycle derived from pollen and insect remains. Palaeogeogr. Palaeoclimatol. Palaeoecol. 103, 73–93.
Helmens, K.F., 2014. The Last Interglacial-Glacial cycle (MIS 5-2) re-examined based on long proxy records from central and northern Europe. Quat. Sci. Rev. 86, 115–143.
Henderson, G.M., Anderson, R.F., 2003. In: Bourdon, B., Henderson, G.M., Lundstrom, C.C., Turner, S.P. (Eds.), The U-series Toolbox for Palaeoceanography. Uranium Series Geochemistry. Geochemical Society and Mineralogical Society of America, Washington), p. 656.
Hill, P., De Deckker, P., Exon, N., 2005. Geomorphology and evolution of the gigantic Murray Canyons on the Australian southern margin. Aust. J. Earth Sci. 52, 117–136.
Hiscock, P., 2017. Discovery curves, colonisation and Madjedbebe. Aust. Archaeol. 83, 168–171.
Hoogakker, B., Elderfield, H., Oliver, K., Crowhurst, S., 2010. Benthic foraminiferal oxygen isotope offsets over the last glacial-interglacial cycle. Paleoceanography 25, PA4229. https://doi.org/10.1029/2009PA001870.
Jouzel, J., et al., 2007. Orbital and millennial Antarctic climate variability over the past 800,000 years. Science 317 (5839), 793–797.
Kaiser, J., Lamy, F., Hebbeln, D., 2005. A 70-kyr sea surface temperature record off southern Chile (Ocean Drilling Program site 1233). Paleoceanography 20, PA4009. https://doi.org/10.1029/2005PA001146.
Kalm, V., Mahaney, W.C., 2011. Late Quaternary glaciations in the Venezuelan (merida) Andes. Dev. Quat. Sci. 15, 279–298.
Kershaw, A.P., Bulman, D., Busby, J.R., 1994. An examination of modern and pre-European settlement pollen samples from southeastern Australia: assessment of their application to quantitative reconstruction of past vegetation and climate. Rev. Palaeobot. Palynol. 82, 83–96.
Kindler, P., Guillevic, M., Baumgartner, M., Schwander, J., Landais, A., Leuenberger, L., 2014. Temperature reconstruction from 10 to 120 kyr b2k from the NGRIP ice core ice core. Clim. Past 10, 887–902.
Kucera, M., Schneider, R., Weinelt, M., 2005. MARGO – Multiproxy approach for the reconstruction of the glacial ocean surface. A special issue. Quat. Sci. Rev. 24, 813–1107.
Lambeck, K., Purcell, A, A., Zhao, J, J., Svensson, N.-O., 2010. The Scandinavian ice sheet: from MIS 4 to the end of the Last Glacial Maximum. Boreas 39, 410–435.
Lambert, F., et al., 2008. Dust2climate couplings over the past 800,000 years from the EPICA Dome C ice core. Nature 452, 616–619.
Lambert, F., et al., 2015. Dust fluxes and iron fertilization in Holocene and last glacial maximum climates. Geophys. Res. Lett. 42, 6014–6032.
Larsen, N.K., Knudsen, K.L., Krohn, C.F., Kronborg, C., Murray, A.S., Nielsen, O.B., 2009. Late Quaternary ice sheet, lake and sea history of southwest Scandinavia – a synthesis. Boreas 38, 732–761.
Lisiecki, L.E., Raymo, M.E., 2005. A Pliocene-Pleistocene stack of 57 globally distributed benthic $\delta^{18}O$ records. Paleoceanography 20, PA1003. https://doi.org/10.1029/2004PA001071.
Lisiecki, L.E., Stern, J.V., 2016. Regional and global benthic $\delta^{18}O$ stacks for the last glacial cycle. Paleoceanography 31, 1368–1394. https://doi.org/10.1002/2016PA003002.
Lopes dos Santos, R.A., Wilkins, D., De Deckker, P., Schouten, S., 2012. Late Quaternary productivity changes from offshore Southeastern Australia: a biomarker approach. Palaeogeog. Palaeoclimat. Palaeoecol. 363–364, 48–56.
Lopes dos Santos, R.A., De Deckker, P., Hopmans, E.C., Magee, J.W., Mets, A., Sinninghe Damste, J., Schouten, S., 2013a. Abrupt vegetation change after the Late Quaternary megafaunal extinction in southeastern Australia. Nat. Geosci. 6, 627–631.

Lopes dos Santos, R.A., Spooner, M.I., Barrows, T.T., De Deckker, P., Sinninghe Damste, J., Schouten, S., 2013b. Comparison of organic ($U^{K'}_{37}$, TEX^{86}, LDI) and faunal proxies (foraminiferal assemblages) for reconstruction of late Quaternary sea surface temperature variability from offshore southeastern Australia. Paleoceanography 28, 1–11.
Magee, J.W., Miller, G.H., Spooner, N.A., Questiaux, D., 2004. Continuous 150 k.y. monsoon record from Lake Eyre, Australia: insolation-forcing implications and unexpected Holocene failure. Geology 32, 885–888.
Mangerud, J., Gullencreutz, R., Øystein, L., Svendsen, J.I., 2011. Glacial history of Norway. Dev. Quat. Sci. 15, 279–298.
Markle, B.R., et al., 2016. Global atmospheric teleconnections during Dansgaard-Oeschger events. Nat. Geosci. 10, 36–40.
McCarthy, A., Mackintosh, A., Rieser, U., Fink, D., 2008. Mountain Glacier Chronology from Boulder Lake, New Zealand, indicates MIS 4 and MIS 2 ice advances of similar extent. Arctic Antarct. Alpine Res. 40, 695–708.
Mejdahl, V., 1979. Thermoluminescence dating: beta-dose attenuation in quartz grains. Archaeometry 21, 61–72.
Middleton, J.F., Bye, J.A.T., 2007. A review of shelf-slope circulation along Australia's southern shelves: Cape Leeuwin to Portland. Prog. Oceanogr. 75, 1–41.
Miller, G.H., Fogel, M.L., 2016. Calibrating $\delta^{18}O$ in *Dromaius novaehollandiae* (emu) eggshell calcite as a paleo-aridity proxy for the Quaternary of Australia. Geochem. Cosmochim. Acta 193, 1–13.
Miller, G.H., Fogel, M.L., Magee, J.W., Gagan, M.K., 2016. Disentangling the impacts of climate and human colonization on the flora and fauna of the Australian arid zone over the past 100 ka using stable isotopes in avian eggshell. Quat. Sci. Rev. 151, 27–57.
Müller, U.C., Pross, J., Tzedakis, P.C., Gamble, C., Kotthoff, U., Schmiedl, G., Wulf, S., Christanis, K., 2011. The role of climate in the spread of modern humans into Europe. Quat. Sci. Rev. 30, 273–279.
Murray, A.S., Wintle, A.G., 2000. Luminescence dating of quartz using an improved single-aliquot regenerative-dose protocol. Radiat. Meas. 32, 57–73.
Niebler, H.-S., Gersonde, R., 1998. Planktic foraminiferal transfer function for the southern South Atlantic Ocean. Mar. Micropaleontol. 34, 213–234.
Norman, K., Inglis, J., Clarkson, C., Faith, J.T., Shulmeister, J., Harris, D., 2018. An early colonisation pathway into northwest Australia 70-60,000 years ago. Quat. Sci. Rev. 180, 229–239.
O'Connell, J.F., et al., 2018. When did H*omo sapiens* reach southeast Asia and Sahul. Proc. Natl. Acad. Sci. Unit. States Am. https://doi.org/10.1073/pnas.1808385115.
Oksanen, J.F., et al., 2016. Vegan: Community Ecology Package. R Package 84.
Olley, J.M., De Deckker, P., Roberts, R.G., Fifield, L.K., Yoshida, H., Hancock, G., 2004. Optical dating of deep-sea sediments using single grains of quartz: a comparison with radiocarbon. Sediment. Geol. 169, 175–189.
Parker, F.F., 1962. Planktonic foraminiferal species in Pacific sediments. Micropaleontology 8, 219–254.
Perner, K., Moros, M., De Deckker, P., Blanz, T., Wacker, L., Telford, R., Siegel, H., Schneider, R., Jansen, E., 2018. Heat export from the tropics drives mid to late Holocene palaeoceanographic changes offshore southern Australia. Quat. Sci. Rev. 180, 96–110.
R Core Team, 2016. A Language and Environment for Statistical Computing. R Foundation for Statistical Computing, Vienna, Austria. https://www.R-project.org/2016.
Sawagaki, T., Aoki, T., 2011. Late Quaternary glaciations in Japan. Dev. Quat. Sci. 15, 1013–1021.
Schaefer, J.M., et al., 2015. The southern glacial maximum 65,000 years ago and its unfinished termination. Quat. Sci. Rev. 114, 52–60.
Spooner, M.I., De Deckker, P., Barrows, T.T., Fifield, L.K., 2011. The behaviour of the Leeuwin Current offshore NW Australia during the last five glacial–interglacial cycles. Global Planet. Change 75, 119–132.
Stenni, B., et al., 2010. The deuterium excess records of EPICA Dome C and Dronning Maud Land ice cores (East Antarctica). Quat. Sci. Rev. 29, 146–159.
Stockhecke, M., et al., 2016. Millennial to orbital-scale variations of drought intensity in the Eastern Mediterranean. Quat. Sci. Rev. 133, 77–95.
Stuut, J.-B., Temmesfeld, F., De Deckker, P., 2014. A 550 kyr record of aeolian activity near North 2014. A 550 ka record of aeolian activity near North West Cape, Australia: inferences from grain-size distributions and bulk chemistry of SE Indian Ocean deep-sea sediments. Quat. Sci. Rev. 83, 83–94.
Tanaka, T., et al., 2000. JNdi-1: a neodymium isotopic reference in consistency with La Jolla neodymium. Chemical Geolology 168, 179–181.
Tierney, J., deMenocal, P.B., Zander, P.D., 2017. A climatic context for the out-of-Africa migration. Geology 45, 1023–1026.
Timmermann, A., Friedrich, F.T., 2016. Late Pleistocene climate drivers of early human migration. Nature 538, 92–95.
Tjallingii, R., Röhl, U., Kölling, M., Bickert, T., 2007. Influence of the water content on X-ray fluorescence core-scanning measurements in soft marine sediments. Geochemistry Geophysics Geosystems 8, Q02004. https://doi.org/10.1029/2006GC001393.
Uemura, R., Masson-Delmotte, V., Jouzel, J., Landais, A., Motoyama, H., Stenni, B., 2012. Ranges of moisture-source temperature estimated from Antarctic ice cores stable isotope records over glacial–interglacial cycles. Clim. Past 8, 1109–1125.
van der Kaars, S., De Deckker, P., 2002. A Late Quaternary pollen record from deep-sea core Fr10/95, GC17 offshore Cape Range Peninsula, northwestern Western Australia. Rev. Palynol. Palaeob. 120, 17–39.
van der Kaars, S., Bassinot, F., De Deckker, P., Guichard, F., 2010. Changes in monsoon and ocean circulation and the vegetation cover of southwest Sumatra through the last 83,000 years: the record from marine core BAR94-42. Palaeogeogr. Palaeoclimatol. Palaeoecol. 296, 52–78.
van der Kaars, S., Miller, G.H., Turney, C.S.M., Cook, E.J., Nurnberg, D., Schonfeld, J., Kershaw, A.P., Lehman, S.J., 2017. Humans rather than climate the primary cause of Pleistocene megafaunal extinction in Australia. Nat. Commun. 8 https://doi.org/10.1038/ncomms14142.
Veres, D., et al., 2013. The Antarctic ice core chronology (AICC2012): an optimized multi-parameter and multi-site dating approach for the last 120 thousand years. Clim. Past 9, 1733–1748.
Veth, P., 2017. Breaking through the radiocarbon barrier: Madjedbebe and the new chronology for Aboriginal occupation of Australia. Aust. Archaeol. 83, 165–167.
WAIS Divide Project Members, 2015. Precise interpolar phasing of abrupt climate change during the last ice age. Nature 520, 661–665.
Wang, Y.I., Cheng, H., Edwards, R.L., An, X.S., Shen, C.-C., Dorale, J.A., 2001. Resolution Absolute-dated late Pleistocene monsoon record from Hulu cave, China. Science 294, 2345–2348.
Weltje, G.J., Tjallingii, R., 2008. Calibration of XRF core scanners for quantitative geochemical logging of sediment cores: theory and application. Earth Planet Sci. Lett. 274, 423–438.
Woillard, G.M., 1978. Grande Pile peat bog: a continuous pollen record for the last 140,000 years. Quat. Res. 9, 1–21.
Wood, R., 2017. Comments on the chronology of Madjedbebe. Aust. Archaeol. 83, 172–174.